NTNU

Norwegian University of
Science and Technology

# Numerical modeling of fracture initiation using plasticity models

Bernardo Gebus

Petroleum Geosciences
Submission date: August 2018
Supervisor: Andreas Bauer, IGP

Norwegian University of Science and Technology
Department of Geoscience and Petroleum

*to all who have had an impact on my life*

# Abstract

Nowadays hydraulic fracturing is a key part of the oil and gas industry to enhance the field's production. Therefore, is important to understand how fractures initiate and how to extract important information from them for further models. The aim of this work is to provide some insights about how the pressure declines with time during a Micro/minifrac test, discuss different techniques for minimum stress determination, and to create a numerical modeling to determine the fracture initiation using plastic models. To accomplish these goals the first part of the work is a theoretical review, in which it can be found the factor that controls the behavior of the pressure decline, followed by fundamentals and advantages of two methods for minimum stress estimation (system stiffness approach and G function). The second objective, is to perform the numerical model by mimicking a typical rock undergoing a normal stress regime at 3000 m depth with a well in the center of the model of 0.3 m radio, afterwards a mesh was built in which the cell size varies depending on the location of the elements, being 0.02m at the wellbore wall and 0.25m at the edge of the model. During each simulation, the pressure inside the well is increased at different injection stages, simulating a fracturing operation. The rock properties are constant during all the simulations besides the hardening rule. It was found that only by changing the hardening rule is unlikely to reach the tensile failure criteria and initiate the fracture; as a matter of fact, at the highest well pressure, it was noticed a stress cage that builds up tangential stress making more difficult to fracture the rock. Another important part of this work was to assess the effect of the packer on the rock, the results show a plastic zone deformation that goes beyond the packer and generates some damage to the rock above and below the packers.

# Preface

This thesis was prepared as part of a two year master study in Petroleum Geosciences at the Norwegian University of Science and Technology (NTNU), to complete an *Master of Science* (MSc) degree in petroleum geophysics. The study was accompanied in collaboration with SINTEF Industry, under supervision of Andreas Bauer (SINTEF).

# Table of Contents

# List of Tables

# List of Figures

Chapter 1

# Introduction

The fluctuating prices of the oil an gas of the past few years led to the operators companies to improve their operational efficiency for maximal production. Hydraulic fracturing has and has had a key role in the increment of production for many years in the industry by making profitable reservoir with low permeability or bypassing the damage zone. In order to execute the hydraulic fracturing in an optimum way the fracture has to be previously designed with the objective of preparing pump, tubing, proppant, and fluid, among other factor (Michael J. Economides (2007)). Of all the parameter that takes place during the design stage of a fracture operation the fracture initiation pressure and the minimum horizontal stress magnitude play a key role. Normally to determine these parameter a micro/minifrac test is performed before the actual fracturing job to ensure the model correspond to the reality.

Fracture design models often use commonly elastic or poroelastic models (Nordgren et al. (1972), Charlez et al. (1997), Valkó et al. (1997)), which could lead to a significant difference between the theoretical fracture initiation pressure and the reality of the fracture operation in rocks that exhibit an inelastic behavior. To overcome this weakness usually a more advanced model needs to be considered, as well as incorporate realistically the nonlinear behavior of the rocks.

For a long time plastic models have been incorporated in different area of material, rocks and soil mechanics. Particularly in the oil and gas industry the effects of hardening/ softening of rocks have been quantified in core plugs aiming to applications on wellbore stability, sanding and reservoir scale application (Bradford et al. (1994), Chen et al. (2016), Risnes et al. (1998), Han et al. (2005)).

Regarding hydraulic fracturing, there have been several studies performing finite element analysis for fracture propagation (Ingraffea et al. (1976), Sepehri et al. (2015)) or highlighting the importance of stress cages for controlling mud losses due to hydraulic or natural fractures. (Feng et al. (2015), Alberty et al. (2004)).

This work is divided into two main parts. The first part is a theoretical review of the mini/microfrac test with special emphasis on how the minimum horizontal stress can be determined through pressure decline analysis and several ways to do so. The second part is a numerical modeling analysis of the behavior of plastic materials undergo high pressure to simulate fracture initiation situation.

The approach of this work consists on performing a finite element analysis in a model built to recreate a typical rock undergoing a normal stress regime at 3000m depth with an already drill borehole of 0.3m radio a hardening rule is set and the pressure inside the wellbore is increased to emulate a fracture operation. The goal is to determine the effect of the plastic model on the stresses around the borehole, also to determine if under this kind of model is possible to reach the tensile failure criteria and lastly quantify the effects that the packer could have in a microfrac operation.

The outline of this work starts by presenting the theoretical concept regarding plasticity theory, followed by Chapter 3 in which is presented a theoretical review of micro/minfrac test describing the behavior of the pressure decline curve and interpretation of minimum horizontal stress. Chapter 4 describes the implemented methodology during the project. The results and analysis are presented in Chapter 5, and finally, Chapter 6 are shows the most important remarks and conclusions.

Chapter 2

# Theory

## 2.1 Plasticity

The theory of linear elasticity is useful for modelling materials which undergo small deformations and which return to their original configuration upon removal of the load. Almost all real materials will experience some permanent deformation, which remains after removal of the load. With metals, rock or any material, important permanent deformations will usually occur when the stress exceed some critical value, called the yield stress.

Elastic deformations are reversible; the energy used in the deformation is stored as elastic strain energy and is completely recovered after releasing the stress. Permanent deformations involve losing of energy; these processes are known as irreversible, in the sense that the original state can be reached only by the expenditure of more energy.

The classical theory of plasticity described materials which at the beginning deform elastically but starts to deform plastically after reaching the yield stress. In metals and other crystalline materials the manifestation of plastic deformations at the micro-scale level is because of the movements and migration of grain boundaries on the micro-level. In sands and other granular materials, plastic flow is due to the permanent reorganization of individual particles and to the irreversible crushing of individual particles Kelly (2013).

The prediction of at which stress state the rock will fail is a meaningful phenomenon for applications in civil engineering, petroleum industry, among others. Rock failure is a complex phenomenon which is still not fully understood. A failure point can be defined fairly easily in a uniaxial test in Fig. 2.1. The situation is not that clear for the higher confining pressures as shown in Fig 2.2, the increase in the confining pressure gradually decreasing of the stiffness of the material, but increases the bearing load capabilities as the strain increase. Thus the material cannot be considered as completely failed, although it has been significantly altered at this stage. Fjaer et al. (2008)

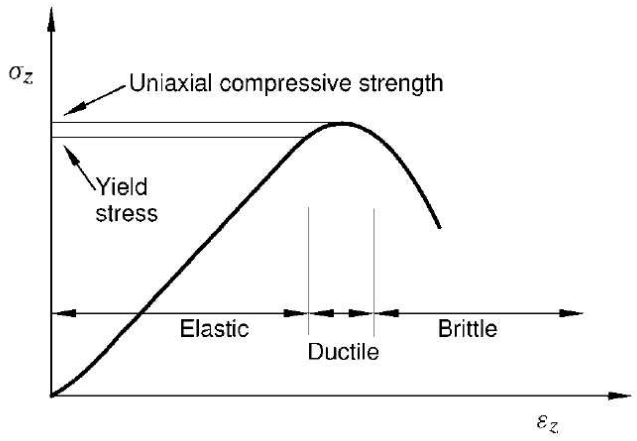


**Figure 2.1:** Sketch of stress versus deformation in a uniaxial compression test.

Tresca in 1864 had the first approach to plasticity theory, by an experiment with metals extrusion and published his well-known yield criterion that will be discussed on section 2.2.1. Additional progress in yield criteria and plastic flow rules were made in the following years. The 1940s; Prager, Hill, Drucker, and Koiter among others brought together many fundamental aspects of the theory into a single framework. The arrival of powerful computers in the 1980s and 1990s provided the impulse to develop the theory further, giving it a more rigorous basis founded on thermodynamic principles, and bring it the need to study many numerical and computational aspects to the plasticity problem. Kelly (2013)

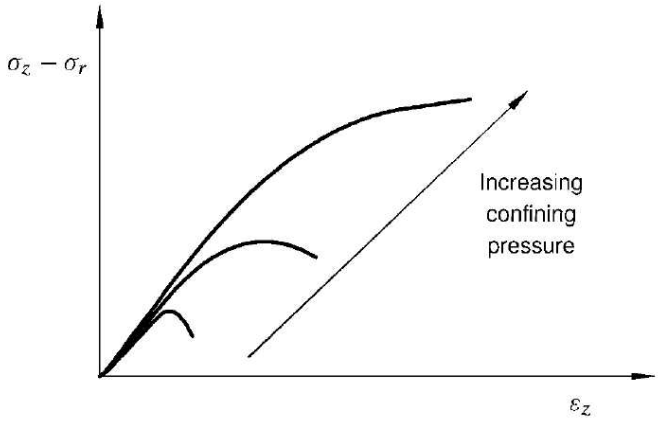


**Figure 2.2:** Triaxial testing: typical influence of the confining pressure on stress vs strain relationship.

The stress-strain curve for a rock subjected to a uniaxial compression can be divided theoretically into several regions (Figure 2.3). In region OAB, the curve is almost linear. The curve continues to growth in region BC, with a change in the slope. The strain reaches a maximum at C, afterward it falls during the course of region CD. In the first region, OAB, the behavior is nearly elastic, loading and unloading in this region will not produce permanent deformation in the framework or properties of the rock. In the second region, BC, the slope of the stress-strain curve, also known as the tangent modulus, decreases gradually to zero as the stress increases. In this region (BC), irreversible changes take place in the rock, and following cycles of loading and unloading would show hysteresis curves, an unloading cycle such as PQ that starts in region BC would provoke permanent strain $\varepsilon o$ when the stress reaches zero. If the rock is reloaded, a path such as QR would be drew out until rejoins it, at a stress greater than the stress at P.

The third region CD, starts at the point of maximum stress C and has a negative slope; in this region the ability of the rock to sustenance a load has decreased. This region of the stress-strain curve is not reached in a testing machine in which the stress is the controlled variable, on those cases a violent failure of the specimen will occur near point C, commonly referred as a uniaxial compressive strength. J. C. Jaeger and Zimmerman (2007)

The second region, BC, the behavior of the rock is identified as a plastic behavior or ductile state, or simply to be ductile. As indicated previously this behavior is characterized by the capability of the rock to support greater loads as it deforms. The range of stresses in which a rock shows elastic or plastic behavior depends on the mineralogy, microstructure, and also on factors such as the temperature.

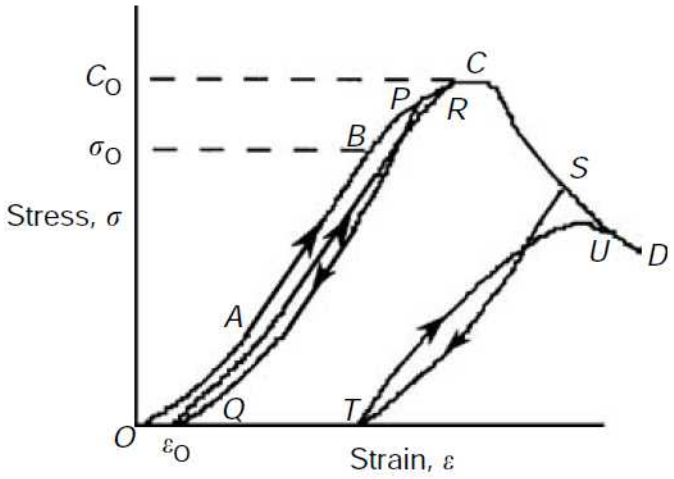


**Figure 2.3:** Complete stress-strain curve for a rock under compression

After exceeding the elastic limit (point B), the material goes through plastic flow. Further increases in stress are usually required to preserve the plastic flow and an increase in the deformation; this phenomenon is known as hardening (see section 2.2.3).

## 2.2 Plasticity Theory

According to Kelly (2013) the plasticity theory for solid materials is founded in the following assumption:

- The response is independent of rate effects.
- The material is incompressible in the plastic range.
- There is no Bauschinger effect (Bauschinger effect represents loss of isotropic behavior in strength-strain behavior produced due to deformation produced in metallic materials).
- The yield stress is independent of hydrostatic pressure.
- The material is isotropic.

The first two items will usually be very good approximations, the other three may or may not be, depending on the material and conditions. For example, normally metals will be assumed to be isotropic. Nevertheless, after large plastic deformation, however, for example in rolling, the material will have become anisotropic: there will be distinct material directions and asymmetries.Is important to notice that Kelly (2013) is describing the plasticity in metals, beside the fact that usually metals are tested under tension and rock under compaction, the main difference in behavior is that rocks are porous material.

The theory of plasticity is based on four major concepts:

1. Plastic strain. The total strain increase associated with a stress increment is presumed to consist of an elastic part and a plastic part:

$$d\varepsilon_{ij} = d\varepsilon^e_{ij} + d\varepsilon^p_{ij} \tag{2.1}$$

d$\varepsilon^e_{ij}$ is related to the stress increment by traditional elasticity theory, and will disappear when the stress is released. The plastic strain d$\varepsilon^p_{ij}$ is a permanent deformation, and will remain when the stress is relieved.

2. A yield criterion. Yield as the point at which permanent changes occur in the rock. Thus, the yield point characterizes the onset of plastic deformation. Then, yield can be defined more accurately than failure. A yield criterion is similar to the failure criteria and describes the surface in stress space where plasticity began.

3. A flow rule. The flow rule describes the way that plastic strains change for a given loading situation.

4. A hardening rule. A rock under given conditions may withstand increasing load after the initial failure. This is described by the hardening rule. The hardening (or, alternatively, the softening) may be understood as a change of the yield surface in principal stress space. This can be defined by changing Eq. 2.2 to

$$f(\sigma'_1, \sigma'_2, \sigma'_3, \kappa) = 0 \tag{2.2}$$

where $\kappa$ is a parameter describing the hardening effects.

For rocks that are loaded below the yield stress, the stress-strain behavior is normally idealized as having a linear relationship between stress and strain, as indicated in the previous section. For rocks that are loaded beyond the yield point, it is necessary to characterize the stress-strain behavior in the region BC of Figure 2.3.

Several idealizations of the plastic behavior of a material can be made (see Figure 2.4). The first one is called plastic behavior with strain hardening. It consists of a linear strain-stress relationship until the yield point, after the yield stress $\sigma_0$ is reached, the stress-strain curve continues to rise but with a gentler slope. The stress $\sigma_0$ is known as the yield stress under uniaxial loading (Figure 2.4a). A yet simpler idealization, in which the stress remains at $\sigma_0$ as the strain continues to increase. A material that obeys a stress-strain law such as that shown in Figure 2.4b. is known as elastic-perfectly plastic. An additional simplification, in which the elastic strains are ignored entirely and assumed to be negligible compared to the plastic strains, is that

of a rigid-perfectly plastic material (Figure 2.4c).J. C. Jaeger and Zimmerman (2007)

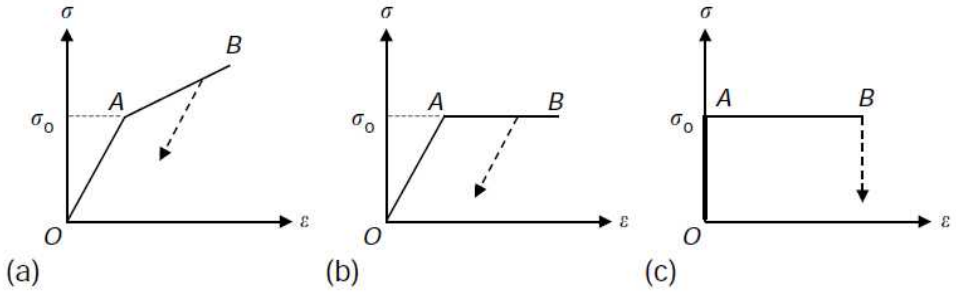


**Figure 2.4:** Idealized uniaxial stress-strain curves: (a) elastic plastic with strain hardening, (b) elastic-perfectly plastic, and (c) rigid-perfectly plastic. Unloading curves are shown as dashed lines.

### 2.2.1 Yield Criteria

Before going into a detailed definition of the yield criteria is important to give at least a basic definition of shear failure. Shear failure occurs when the shear stress along some plane in the sample is sufficiently high. Eventually, a fault zone will develop along the failure plane, and the two sides of the plane will move relative to each other in a frictional process. Failure occurs along a clearly defined plane of fracture, this plane is typically inclined at an angle less than 45° from the direction of $\sigma_1$ (the axial direction, in this case). This plane is characterized by shearing movement along its surface and is denoted as a shear fracture. If the confining pressure is increased, so that the rock has fully ductile behavior, a network of small shear fractures appears, together with plastic deformation of the individual rock grains. J. C. Jaeger and Zimmerman (2007).

Now, we can assume that yield will occur at a particle when some combination of the stress components reaches some critical value.

$$F(\sigma_{11}, \sigma_{12}, \sigma_{13}, \sigma_{22}, \sigma_{23}, \sigma_{33}) = \kappa \tag{2.3}$$

F is some function of the 6 independent components of the stress tensor and $\kappa$ is a material property which can be determined experimentally. the function F will also contain other parameters that must be found experimentally.

On the other hand, it is useful to express yield criteria in terms of principal stresses. Assuming that the principal stresses are known everywhere, $(\sigma_1, \sigma_2, \sigma_3)$. Yield must depend in some way on the microstructure on the direction of the axes $x_1, x_2, x_3$, but this information is not contained in the three numbers $(\sigma_1, \sigma_2, \sigma_3)$. Thus we express the yield criterion in terms of principal stresses in the form

$$F(\sigma_1, \sigma_2, \sigma_3, n_i) = \kappa \tag{2.4}$$

Where $n_i$ represent the principal directions. These give the orientation of the principal stresses relative to the material directions $x_1, x_2, x_3$. If the material is isotropic, the response do not depends of some material direction, then the yield criterion can be conveyed in the simple form. Kelly (2013).

$$F(\sigma_1, \sigma_2, \sigma_3) = \kappa \tag{2.5}$$

### Mohr Coulomb criterion

It is established that the frictional force that acts against the relative movement of two objects in contact is governed by on the force that presses the bodies together. Thus, it is realistic to accept that the critical shear stress ($\tau_{max}$) for which shear failure occurs, depends on the normal stress ($\sigma'$) acting over the failure plane. That is:

$$|\tau_{max}| = f(\sigma') \tag{2.6}$$

This assumption is called Mohrs hypothesis.

In the $\tau - \sigma'$ plane, Eq. 2.6 defines a line that separates a safe zone from a failure region, and Eq. 2.6 might be consider as a representation of the failure surface in the $\tau - \sigma'$ plane. The line is often known to as the failure line or the failure envelope. An example is shown in Figure 2.5, where we have also indicated the three principal stresses and the Mohrs circles connecting them

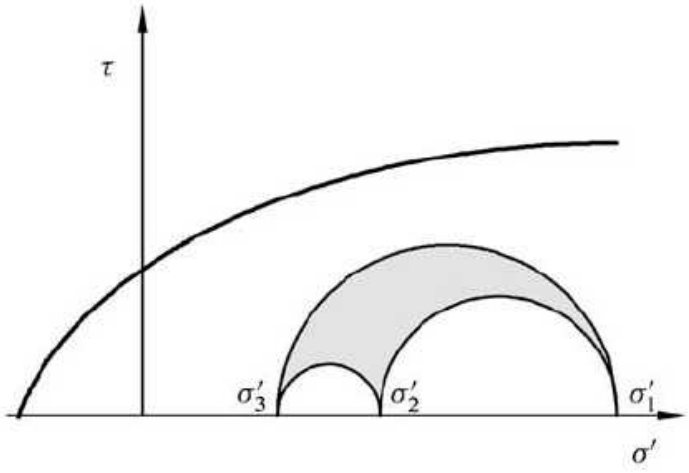


**Figure 2.5:** Failure line, as specified by Eq.2.6, in the shear stressnormal stress diagram. Mohr circles connecting the principal stresses are also shown

The stress state of Figure 2.5 represents a situation with no failure, as no plane within the rock has a combination of $\tau$ and $\sigma'$ that touch the failure line. Assume now that $\sigma'_1$ is increased. The circle form by connecting $\sigma'_1$ and $\sigma'_3$ will expand and eventually reach the failure line. The failure criterion is then satisfied for some plane(s) in the sample, and the sample fails. Note that the value of the intermediate principal stress ($\sigma'_2$) has no influence on this situation.

Since $\sigma'_2$ by definition lies within the range ($\sigma'_3$, $\sigma'_1$), it does not disturb the outermost of Mohr is circles, and therefore it does not affect the failure. So, pure shear failure, as defined by Mohr is supposition, will be governed by the minimum and maximum principal stresses and not on the intermediate stress.

Mohr-Coulomb criterion, which is based on the assumption that f ($\sigma'$) is a linear function of $\sigma'$:

$$|\tau_{max}| = S_0 + \mu\sigma' \tag{2.7}$$

$S_0$ is the inherent shear strength (also called cohesion) of the material.

Here $\mu$ is the coefficient of internal friction. The final term is obviously chosen by analogy with sliding of a object on a surface, which to the first approximation is defined by Amontons friction law:

$$\tau_{max} = \mu\sigma' \tag{2.8}$$

In Figure 2.6 it is drawn the Mohr-Coulomb criterion and a Mohrs circle that touches the failure line. The angle  defined in the Figure is called the angle of internal friction (or friction angle) and is related to the coefficient of internal friction by

$$tan\varphi = \mu \tag{2.9}$$

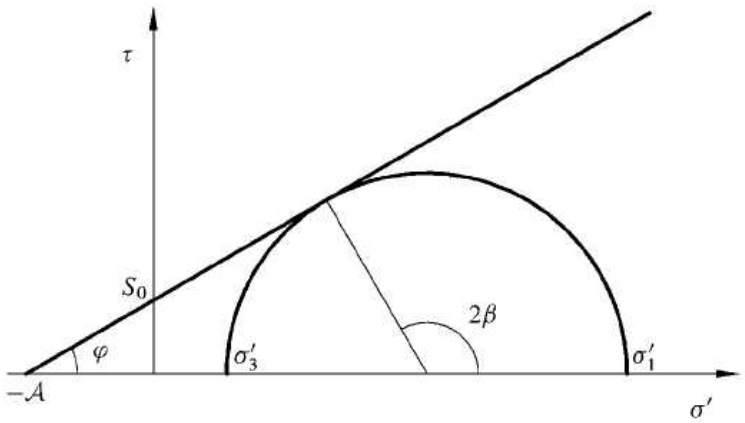


**Figure 2.6:** MohrCoulomb criterion and Mohrs circle showing a critical stress state.

The MohrCoulomb failure surface looks in three dimensional principal stress space as an irregular hexagonal pyramid shape, failure is independent of the intermediate principal stress. To build the surface is necessary to abandon momentarily the convention $\sigma_1' > \sigma_2' > \sigma_3'$. The projection onto $(\sigma_1', \sigma_3')$ plane when $\sigma_1' > \sigma_3'$ and $\sigma_1' < \sigma_3'$ can be represented as two straight lines with symmetry around $\sigma_1' = \sigma_3'$. (figure 2.7a). Similar projection can be perform on the remaining two planes obtaining an irregular hexagon pyramid shape shown on figure 2.7b. The surface is not differentiable at the corners, a fact that may cause problems in numerical calculations involving the criterion. Fjaer et al. (2008).

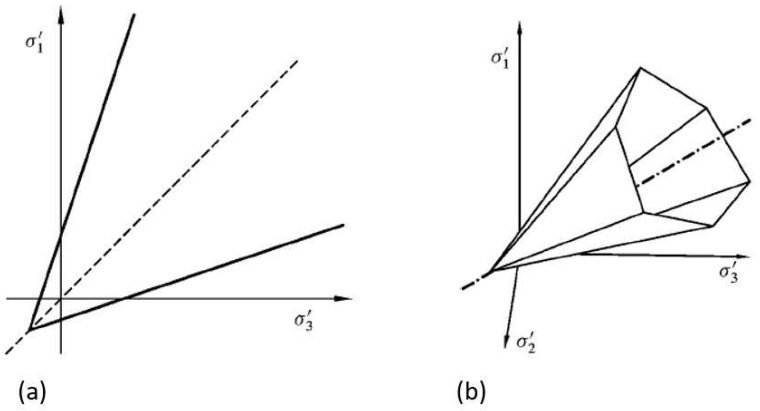


**Figure 2.7:** (a)Projections onto the $(\sigma_1', \sigma_3')$ plane, of the failure surface. Symmetry about the projection of the hydrostatic axis (dashed line). (b) The MohrCoulomb failure surface in principal stress space.

#### Tresca Yield Condition

By choosing specific forms of the function f ($\sigma'$) of Eq. 2.6, various criteria for shear failure are obtained. The simplest possible option is a constant. The resulting criterion is called the Tresca criterion. The criterion basically states that the material will yield when a critical level of shear stress is touched:

$$|\tau_{max}| = \frac{1}{2}(\sigma'_1 - \sigma'_3) = S_0 \tag{2.10}$$

In a Mohr $\tau - \sigma'$ plot the Tresca criterion appears simply as a straight horizontal line.

The Tresca criteria representation on a three-dimensional principal stress space will be six-sided cross-section as the Mohr-Coulomb, but for this criterion, the section will be a regular hexagon. Since the friction angle is zero, the failure surface will be parallel to the hydrostatic axis.

#### Von Mises Yield Condition

The Von Mises criterion states that yield occurs when the principal stresses satisfy the Relation

$$(\sigma'_1 - \sigma'_2)^2 + (\sigma'_1 - \sigma'_3)^2 + (\sigma'_2 - \sigma'_3)^2 = C^2 \tag{2.11}$$

C is a material parameter related to cohesion

The criterion is seen to be identical to the Tresca criterion for $\sigma'_2$ = $\sigma'_1$ or $\sigma'_2$=$\sigma'_3$. Like the Tresca criterion, the von Mises criterion describes a shear failure mechanism where the failure condition is independent of the stress level in the material. The von Mises criterion is commonly used to describe yield in metals. It has however very limited applications for rocks. In a three-dimensional principal stress space the criteria would behave as a cylinder where the center is the hydrostatic axis.Fjaer et al. (2008)

### 2.2.2 Plastic flow

The function of the flow rule is to describe the development of the plastic strain increments. The basic assumption concerning plastic flow states

$$d\varepsilon_{ij} = d\lambda h_{ij}(\sigma'_{kl}) \tag{2.12}$$

Where $\lambda$ is a scalar not indicated by the flow rule. $h_{ij}$ are functions of the stress components. There are two main consequences of Eq. 2.12. First, it claims that the direction of plastic flow is given by the stress state, and is not influenced by the stress increments or by stress gradients. Second, the amount of the plastic strain is not unique. These states make sense intuitively for an perfectly plastic material since the yield stress doesn't change for any magnitude of the plastic strain.

The assumption that plastic strains are independent of stress increments, can be easily explained using the following simple example. Consider a body placed on some surface and

assume that a force close to overcome the static friction between the object and the surface is applied. Now, a small force increment is applied at some angle to the primary force. If the force increment has a component in the direction of the primary force, the static friction will be overcome, and the body will start to move in the direction of the primary force, regardless of the direction of the force increment. Fjaer et al. (2008)

Eq 2.12 places some restrictions on the plastic behavior, nevertheless it is far from a complete explanation which requires a specification of the functions $h_{ij}$. Some hint is found from the fact that plastic deformation is a dissipative process, which implies that

$$\sum_{ij} \sigma'_{ij} d\varepsilon^p_{ij} \geq 0 \tag{2.13}$$

A significant simplification results from the assumption of von Mises (1928), that the$h_{ij}$ s can be derived as the gradient of a function g in stress space:

$$d\varepsilon_{ij} = d\lambda \frac{\partial g}{\partial \sigma'_{ij}} \tag{2.14}$$

The function g is named plastic potential and have to be chosen such that Eq. 2.13 is obeyed. Though the assumption of a plastic potential decreases the necessity for a specification of six functions $h_{ij}$ of six variables to one function g of six variables, it is by no means sufficient to completely specify plastic flow. The plastic potential is also called a non-associated flow rule.

One explanation to the problem is Druckers (1950) description of a stable, work hardening material. Such a material is defined by a harsher version of Eq. 2.13:

$$\sum_{ij} d\sigma'_{ij} d\varepsilon^p_{ij} \geq 0 \tag{2.15}$$

Note that while Eq. 2.13 is a thermodynamic law, meanwhile Eq. 2.15 is not, and thus the consequences resulting from Eq. 2.15 need not be followed by all materials. From Eq. 2.15 Drucker establish that the plastic potential g is identical to the function f describing the yield surface, that is:

$$d\varepsilon^p_{ij} = d\lambda \frac{\partial f}{\partial \sigma'_{ij}} \tag{2.16}$$

This flow rule is known as associated flow-rule. The flow rule is associated with a specific yield criterion. Fjaer et al. (2008).

### Associated Flow Rules

The yield surface f($\sigma'$)=0 is represented as a projection on the $\sigma_1$, $\sigma_3$ plane as a straight line; the material is subjected to the stress state shown in the point A of the figure 2.8. The normal to the yield surface is in the direction df /$\sigma_{ij}$ and so the associated flow rule Eq. 2.16 can be understood as that the plastic strain increment vector is perpendicular to the yield surface, as indicated in the figure 2.8. This is called the normality rule. Kelly (2013)

From the figure we see that

$$d\varepsilon^p_1 = d\lambda \cos\gamma \tag{2.17}$$

$$d\varepsilon_3^p = -d\lambda \sin\gamma \tag{2.18}$$

Therefore

$$d\varepsilon_3^p + d\varepsilon_1^p \tan\gamma = 0 \tag{2.19}$$

For example the Coulomb criterion does not depend on the intermediate principal stress $\sigma_2'$ and then $d\varepsilon_2^p = 0$. The volumetric strain increment $d\varepsilon_{vol}^p = d\varepsilon_1^p + d\varepsilon_2^p + d\varepsilon_3^p$ is then:

$$d\varepsilon_{vol}^p = d\varepsilon_1^p(1 - \tan\gamma) \tag{2.20}$$

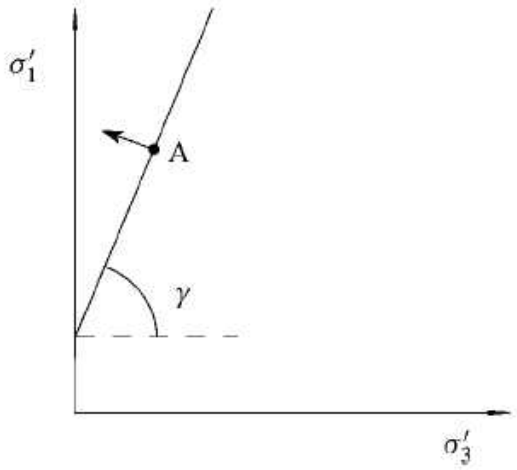


**Figure 2.8:** Associated plastic flow for the Coulomb criterion in a principal stress plot.

For the Coulomb criterion, $\gamma$ is greater than 45, since $\sigma_1$ is greater than $\sigma_3$ and therefore. Due to the sign convention, this means an increase in the volume. This effect is called dilatancy. For perfectly plastic material the dilatancy occurs while the mean stress remains constant. On the other hand, if we consider a linear elastic material, the volume of the sample will change as a result of the mean stress.Fjaer et al. (2008)

#### Non-associated flow

Non-associated plastic flow may occur if the plastic potential is not identical to the yield surface. It is a convenient model to implement aiming to have control on dilatancy without changing the yield surface. A non-associated yield criterion is found by changing the angle in the equation of plastic potential form friction angle to angle of dilatation.

The angle of dilation controls an amount of plastic volumetric strain developed during plastic shearing and is assumed constant during plastic yielding. The value of $\psi$ =0 corresponds to the volume preserving deformation while in shear. A negative value of dilatancy angle is acceptable only for very soft rocks, more similar to loose sands .

### 2.2.3 Hardening

In a uniaxial case, a rock will deform up to yield and then generally harden, in figure2.9 is shown a perfectly-plastic idealization as well as hardening case. In the perfectly plastic material, once the material undergoes a stress state equal to the yield point (A), plastic deformation

will occur, as long as the stress is maintained at Y. If the stress is decreased, elastic unloading will take place. In the hardening case, once yield point is reached, the stress needs to have a continuous increment in order to keep the plastic deformation. If the stress is held constant, for example at B, no additional plastic deformation will occur; neither elastic unloading.

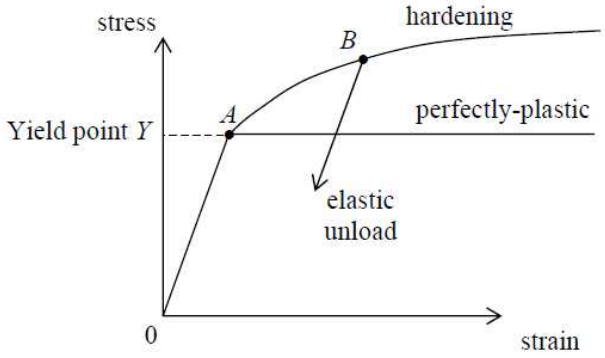


**Figure 2.9:** Uniaxial stress-strain curve

According to Eq 2.5 in three dimensions the hardening can be described as the change on size, shape or position of the yield surface as a function of $\kappa$ parameter related to the plastic strains.

There are two common types of hardening modes (Figure 2.10), isotropic and kinematic hardening. Isotropic hardening occurs when the yield surface change expands or shrinks in a uniform around the hydrostatic axis. On the other hand, kinematic hardening relates to a change in the yield surface in the stress-space axes. In practice, hardening has to be defined by a mixture of the modes or an even more complicated behavior, where different parts of the failure envelop deform in different ways. Kelly (2013)

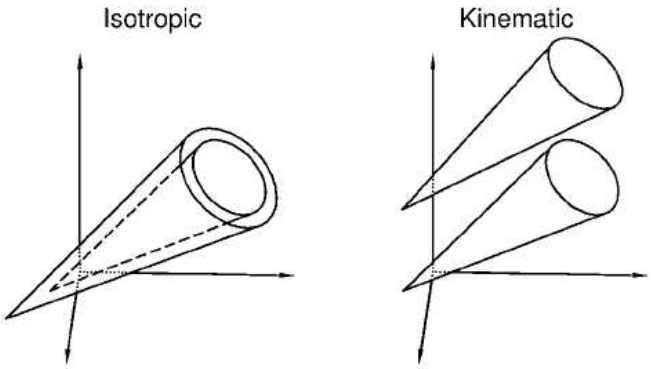


**Figure 2.10:** Isotropic and kinematic hardening in principal stress space.

Chapter 3

# Literature Review

## 3.1 Micro/mini Frac Test

A typical ideal pressure-time recording for a series of micro/minifrac test cycles is shown in Figure 3.1; this indicates a number of short pumping cycles to pressurize a preselected (normally perforated) interval. Each cycle is followed by a shut-in period of about 15-20 min.

A micro/minifrac test consists on adding the pressure in the wellbore, ideally, the fluid pumping into a well occurs at a constant rate and the pressure should increase linearly with time as the volume of the system is fixed. At the pressure where there is a clear departure from a linear increase of wellbore pressure with time (referred to as the LOP, the leak-off point). A clear LOP is approximately equal to the least principal stress. If the LOP is not reached, a limit test, or formation integrity test (LT, or FIT), is said to have been conducted. The peak pressure reached during a micro/minifrac is known as formation breakdown pressure (FBP) and represents the pressure at which unstable fracture is created in the wellbore because volume of the system has increased enough to change the pressurization on the well. As pumping continues at a constant rate, the pumping pressure measured in the well drops below the FBP to a relatively constant value called the fracture pumping pressure (FPP), the pressure associated with propagating the fracture far from the well, the FPP is close to the least principal stress. After abruptly stopping flow into the well, two inflection points are expected on the decline pressure curve. The first one is a sudden drop in pressure and is known as instantaneous shut-in pressure (ISIP), this point normally is easy to interpret. Although the ISIP is often interpreted as an upper limit of the minimum horizontal stress, actually correspond to the created net pressure that keeps the fracture open to flow and should, for small friction losses, be close to the fracture propagation pressure. Bree and Walters (1989), Proskin et al. (1989)

A more accurate measure for the far-field minimum in situ stress, is provided by the fracture closure pressure (FCP). Which corresponds to the fracture fluid pressure at which the fracture width reduces to zero. The FCP corresponds to the second slope inflection point on the post-shut-in pressure decline curve (below the ISIP), this change in slope being attributed to the different leak-off rates over the ”open” and ”closed” fracture faces.

When performing more than one pumping cycle, the pressure build-up curve follows can provide another measurement for the minimum in situ stress. This is called fracture reopening pressure (FRP), to be identified as the pressure at which build-up observed during fluid injec-

tion starts to deviate from a straight line (Figure 3.1). An accurate determination of the FRP is important to use a low injection rate and to bleed off the fluid pressure between cycles in order to obtain a sufficiently large initial reference straight-line portion.

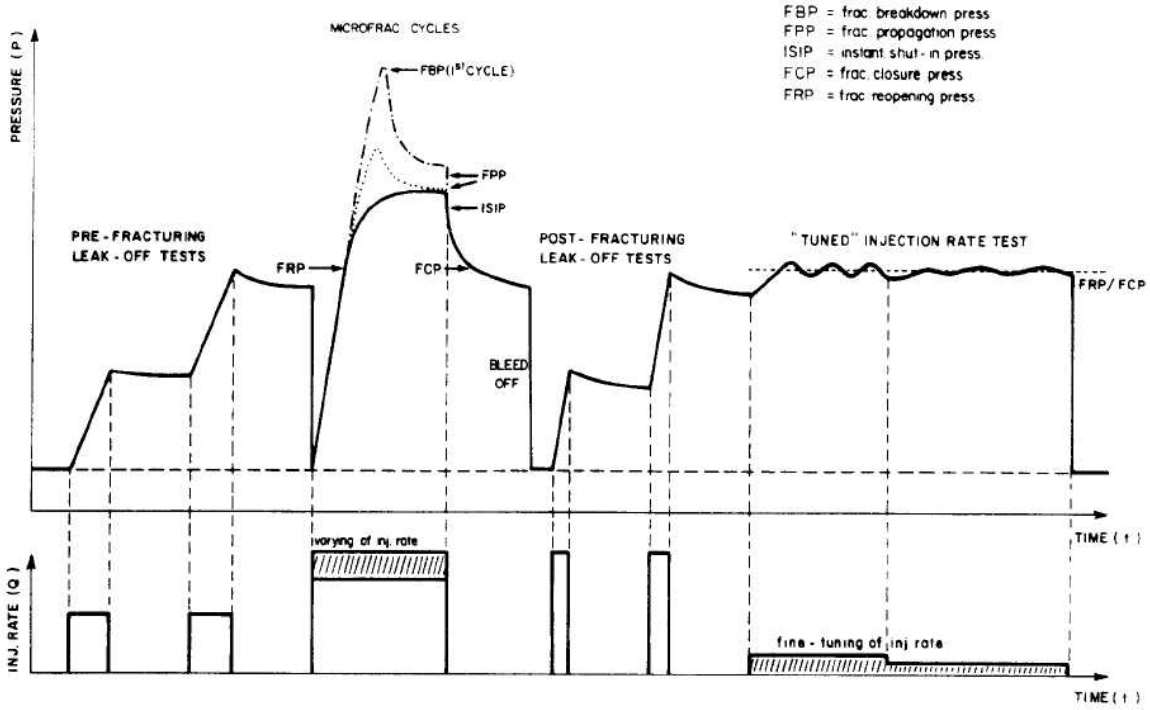


**Figure 3.1:** Sketch of a typical ideal pressure-time recording for a series of micro/minifrac test cycles.

For low rates, the FRP turns out to be close to the FCP, indicating that fracture reopening is not much affected by the near-wellbore stress concentrations. This suggests that the presence of (narrow) conductive channels along the ”closed” fracture surface generally govern the reopening process. (Bree and Walters (1989))

In low leak-off formations (for example low permeability sands, shales, rock salts), an extended shut-in test can take an excessively long time. In such cases, a pump-in/flow-back test is more suitable (see Figure 3.2). This test might also have benefits over the direct test procedure discussed above, after shut-in and after the start of backflow, shows a more easily identifiable slope variation at fracture closure (Figure 3.2). By adjusting flow-back rates over several cycles, optimum conditions can be accomplished.

At high backflow rates, a part of the fracture could pinch off from the well as a result of a high viscous pressure drop close to the mouth of the fracture. The FCP will then agrees to the pressure at which the fracture closes in the near wellbore vicinity and will, for this reason, provide an upper limit for the total minimum in situ stress. The fluid pressure in the remaining, pinched-off, part of the fracture, nonetheless, may remain in excess of the FCP. An indication of this is that, once the well is shut in, the well pressure increases as a consequence of the reopening of the fracture mouth, letting higher-pressure fluids to communicate with the well (Figure 3.2). This reopening of the fracture provides the possibility of detecting a second FCP by initiating the backflow again (possibly at a different flow-back rate).

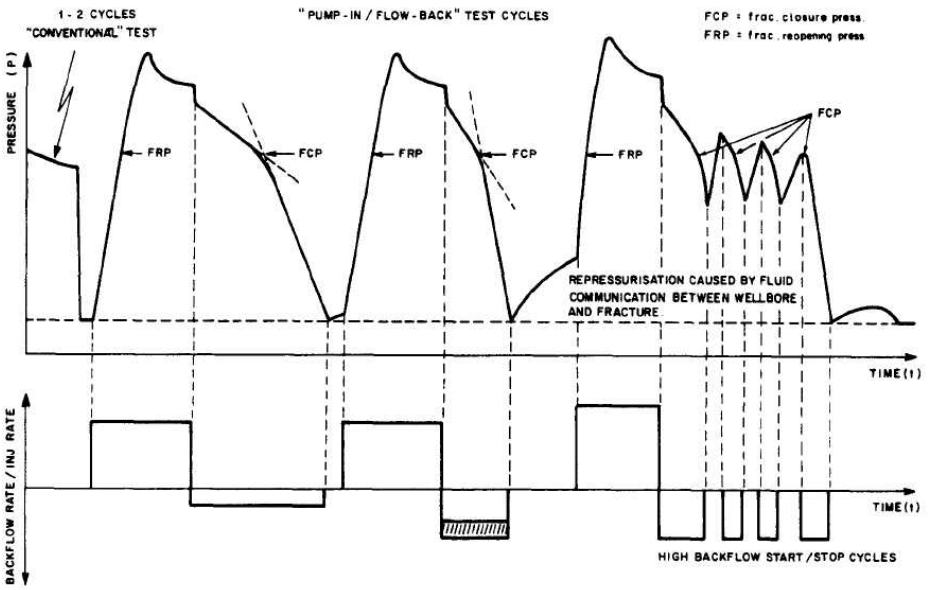


**Figure 3.2:** Sketch of a pressure profile for pump-in/flow-back test.

In the following example carried out at one location in the Netherlands it can be seen schematically the difference between a test conducted with or without backflow. Figures 3.3a-d show several cycles of the test, performend in a sandstone formation, using an injection rate of 10 barrels/min and a fracturing fluid emulsion of kerosene/water gel. Having a formation permeability (0.11 mD) and a low leak-off, no positive identification of an FCP could be made from traditional cycles (no backflow, Fig. 3.3a). At very high backflow rates (Fig. 3.3b), appreciable pinching-off was observed. At low backflow rates (Fig. 3.3c), it was possible to reach at a well-defined FCP. The last cycle (Fig. 3.3d) shows the use of a number of backflow start/stop cycles within one post-shut-in period. Bree and Walters (1989)

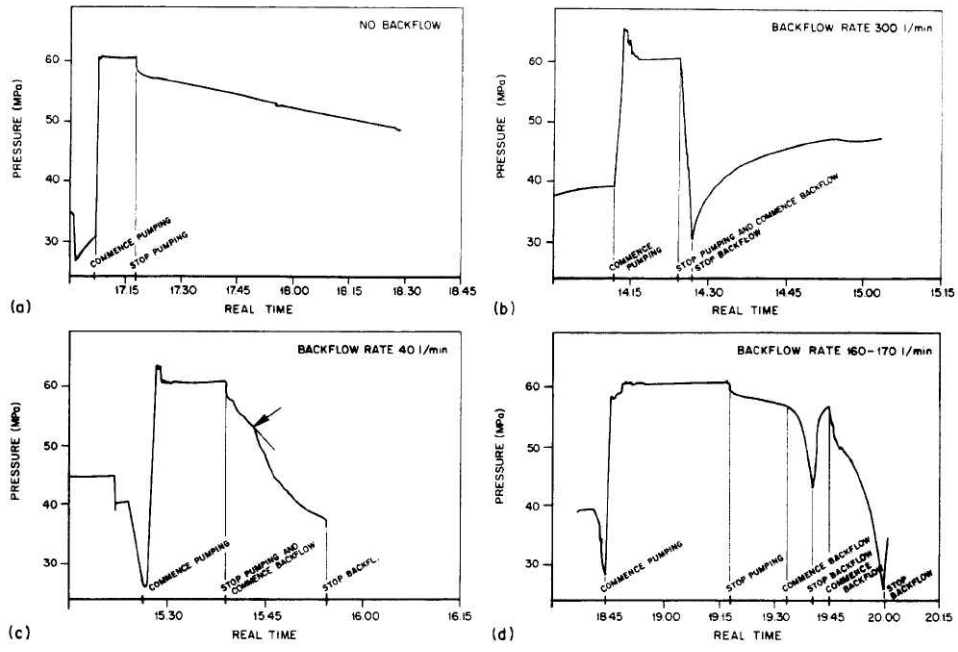


**Figure 3.3:** Example of FCP determination without backflow and with different rate of backflow.

### 3.1.1 Pressure Decline Curve Behavior

As described in the previous section the hydraulic fracturing is used to determine the minimum horizontal stress. Typically is assumed a vertical well and the minimum principal stress is assume to be normal to the borehole direction (figure 3.4. A pressure is applied in a borehole interval (normally separated by two packers). The pressure between the packers is raised by injecting fluid under a constant flow rate until the fracture breakdown pressure is reached.

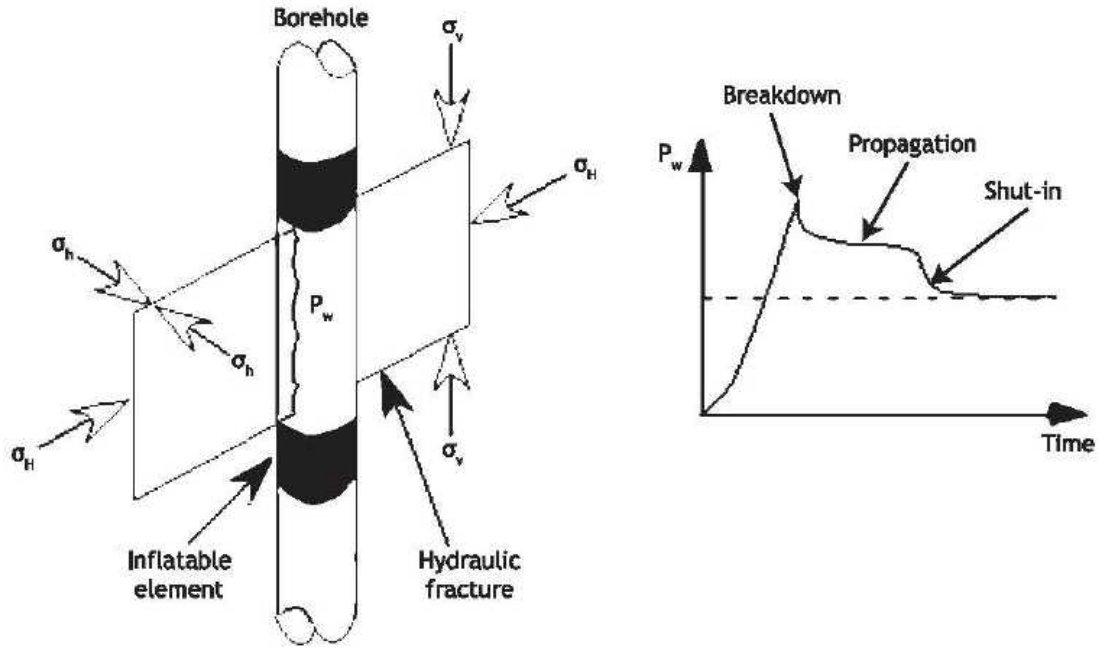


**Figure 3.4:** Schematic presentation of a classical HF test for stress measurement.

Injection continues so that the hydraulic fracture extends away from the well and it may be shown that the fracture extends perpendicularly to the local minimum principal stress direction. To be able to measure the minimum horizontal stress the injection can stop when the fracture tip reaches domains where the stress field is unaffected by the borehole. If the treatment stop before this point it will be measurement the hoop stress (tangential stress) around the borehole. Before shut-in, the injected fluid flows into the fracture from the wellbore toward the fracture tip, and consequently a pressure gradient due to viscous loss exists within the fracture. According to linear fracture mechanics, the stress intensity factor at a fracture tip can never exceed the fracture toughness of the medium containing the fracture, and thus the fracture extends so as to maintain the balance between the two. Hayashi (1991)

At the shut-in, the inflow into the fracture stops and the pressure gradient reduces, causing the pressure in the near of the fracture tip to rise. These forces the make the fracture to keep growing until the fracture fluid pressure decreases to a level for which the stress intensity and the fracture toughness are equal. After shut-in, fluid pressure will be uniform within the fracture and will decrease gradually due to leak-off into the rock causing the fracture aperture to decrease accordingly. Fracture closure begins at its tip and continues toward the well bore. Finally, the fracture closes completely. After that, the fluid may continue to leak off, but only through the wellbore surface. The entire fracture closure process is shown schematically in Figure 3.5.

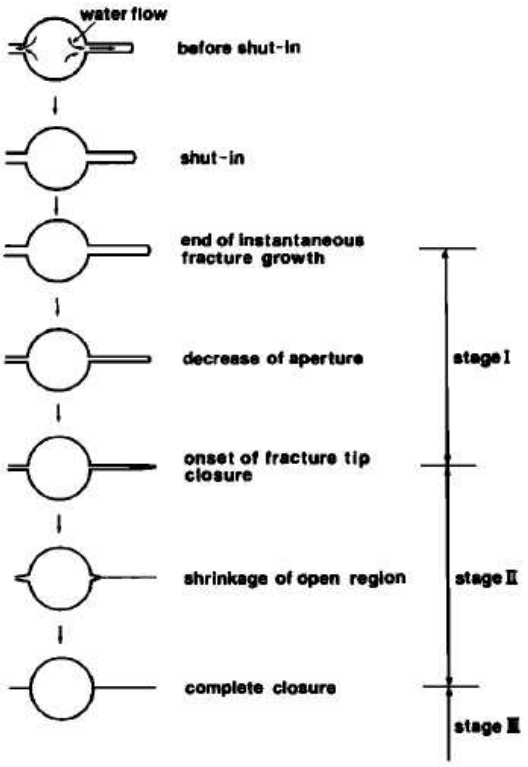


**Figure 3.5:** Different stage in hydraulic fracture closure process.

Hayashi (1991) identify the mains stages that control the pressure time decay during fracture closure. The first stage will be as described previously, during fracture propagation, a pressure gradient exists along the fracture and when injection stops, the initial phase of the pressure decay observed at the borehole wall corresponds to the phase during which the pressure gets uniform along the fracture, up to the fracture tip. Then the fracture surfaces get closer to each other, because of the drop in pressure associated with the flow through the fracture walls and because the fracture keeps extending. During this phase, the two sides of the fracture do not touch each other yet.

The second stage corresponds to the time when the fracture closes progressively, (the area of solid contacts between both faces of the fracture increases with time). It is followed by a third and final stage during which the fracture is mechanically closed so that the pressure decay is only dependent on permeability effects (and possibly leakage of the testing system).

### Fundamentals

The following analysis of the pressure decay curves after shut-in in hydraulic fracturing stress measurements is based on linear theory of elasticity and global mass balance of fracturing fluid after shut-in, uniform average with, fluid loss rate into formation and elapsed time (Howard (1957) and Pattillo (1975)). Based on these characteristics, it was possible to develop a method for the determination of the in situ minimum compressive stress from the pressure time curve.

The basis of the interpretational model for micro/minifrac test analysis comes from the following volume balance equation:

$$Q_{inj}(t) = c\dot{P}[V + v(t)] + \dot{v}(t) + Q_{lO} \tag{3.1}$$

Where
$Q_{inj}(t)$ is the fluid injection rate at surface. $Q_{lo}$(t) is the momentary fluid leak-off rate into the formation. V is the geometrical volume of the pressurized part of the completion'. $v$(t) is the momentary geometrical volume of the fracture. c is the fluid compressibility. P(t) is the bottomhole pressure (BHP).

The dotted letters on the equation correspond to derivatives with respect to time. All friction losses are neglected and it is implicitly assumed that the pressure is uniformly distributed over the fracture. (Alternatively, P(t) represents an average of the pressures prevailing at the well bore and the fracture tip.)Bree and Walters (1989)

During fracture reopening (pressure build-up period) and fracture closing (pressure decline period), zero fracture propagation is assumed and the fracture's response to the pressure is described by a "fracture compressibility"($c_f$) or "fracture compliance" (H):

$$\dot{v}(t) = c_f(t)v(t)\dot{P}(t) = H\dot{P}(t) \tag{3.2}$$

By combining Eq3.1 and Eq3.2 the equation governing the pressure build-up and decline phases reads:

$$\begin{aligned} Q_{inj}(t) &= \dot{P}(t)[cV + c + c_f v(t)] + Q_{lo}(t) \\ &\simeq \dot{P}(t)[cV + H(1 + c/c_f)] + Q_{lo}(t) \end{aligned} \tag{3.3}$$

This equation provides the essentials for a global description of leak-off tests ($Q_{inj}$(t)=O after shut-in, $v$(t)=O), low and constant rate reopening tests ($Q_{inj}$(t)=$Q$), extended shut-in tests ($Q_{inj}$(t)=0 after shut-in) and pump-in/flow-back tests ($Q_{inj}$(t)=$Q_{bf}$ after shut-in, where $Q_{bf}$ denotes the constant backflow rate).

The following results are found for the post-shut-in pressure decline stages connected with extended shut-in tests and backflow tests: Bree and Walters (1989)

prior to fracture closure:

$$\dot{P} = -\frac{Q_{bf} + Q_{lo}(t)}{[cV + (c + c_f(t))v(t)]} = -\frac{Q_{bf} + Q_{lo}(t)}{[cV + H(1 + c/c_f)]} \tag{3.4}$$

after fracture closure:

$$\dot{P} = -\frac{Q_{bf} + Q_{lo}(t)}{c(V + v_{fc})} \tag{3.5}$$

The previous expression takes into account that with the fracture "closed", open conductive channels are still to be expected (the subscript fc pertains to this closed fracture). In a pump-in/flow-back test, in which a constant backflow rate $Q_{bf} \gg Q_{lo}$(t), $Q_{lofc}$(t), the pressure fall-off curve is estimated to be made up of two straight-line portions, their slopes being fully determined by the value of backflow rate choose. Once the fracture is closed a steepening of the slope is anticipated as a result of the loss of the fractures' compliance.

In the conventional extended shut-in test ($Q_{bf}$ = 0), the pressure decline with time rate related with fracture closure is generally less obvious because of the implicit non-linear behavior of the pressure fall-off. A less steep slope is now expected over the closed fracture, where the total area available for leak-off is supposed to be drastically reduced in comparison with the open fracture. The majority of practical case show the characteristic concave-upward pressure decline curves. It should be noted, however, that this trend will be counteracted by the effect of a reducing fracture compliance as the fracture closes. Bree and Walters (1989)

The response of the pressure decay becomes more complicated when the fracture only partly closes, which would result in a less salient reduction of the leak-off area on closure; or when a loss of compliance occurs for the open fracture, for example as a result of the roughness of the fracture faces or of natural induced debris accumulation between the fracture faces. Therefore, it is quite possible to observe both a concave-upward and concave-downward post-shut- pressure decline.

**Characteristics Of Pressure Decrease After Shut-In**

Pressure decrease after shut-in is governed by the following differential equation derived from global mass conservation of the fracturing fluid Hayashi (1991)

$$\frac{dP}{dT} = \frac{\rho_c Q_1}{(d/dP)(\rho_c + V_c + \rho_c V_b + M_H)} \tag{3.6}$$

Where P is the interval pressure, T is the time after the onset of pressurization, Pc is the mass density of the injected fluid in the pressurized interval, Q1 is the volumetric fluid loss rate due to permeation into the rock, Vc is the volume of the hydraulic fracture, VB is the volume of the pressurized interval, and MH is the fluid mass in the tubing connecting the straddle packer system to the pump. The volumetric fluid loss rate can be expressed as Nolte (1986)

$$\begin{aligned} Q_l &= \frac{A_0 C}{(T_0)^{1/2}} 2[(\frac{T}{T_0})^{1/2} - (\frac{T}{T_0} - \frac{A}{A_0})^{1/2}] 2\pi R h_B \frac{C}{T^{1/2}} \\ &= \frac{C(T_0)^{1/2}}{R} \frac{R^3}{T_0} \{a[(\frac{T}{T_0})^{1/2} - (\frac{T}{T_0} - \frac{A}{A_0})^{1/2}] + \frac{b}{(T/T_0)^1/2} \end{aligned} \tag{3.7}$$

$$a = 8\frac{h_c L}{RR'}, b = 2\pi\frac{h_B}{R} \tag{3.8}$$

Where C is the fluid loss coefficient, To is the time at shut-in, R is the well bore radius, ha is the length of the pressurized interval, h c is the fracture height, and L is the fracture length. The areas of fluid permeation from the fracture before and after fracture tip closure as denoted by A0 and A, respectively.

After complete hydraulic fracture closure (stage III), fracture volume is zero, and hence fluid leakage from the fracture surfaces into the rock is negligibly small, so that equations 3.6 and 3.7 become:

$$\frac{dP}{dT} = \frac{\rho_c Q_1}{(d/dP)(\rho_c V_B + M_H)} \tag{3.9}$$

$$Q_l = \frac{C(T_0)^{1/2}}{R}\frac{R^3}{T_0}\frac{b}{(T/T_0)^{1/2}} \tag{3.10}$$

After several approximation Hayashi (1991) found an analytical solution for the first and the third stage of the fracture closure

For the first stage the pressure can be approximated to

$$p \cong \frac{1}{3}(\frac{ka}{\varphi})^2\frac{dt}{dp} + p_1^* \tag{3.11}$$

$$p_1^* = p_1 - \frac{1}{3}\frac{k}{\varphi}a + \frac{2}{3}\frac{k}{\varphi}a\{t_1^{3/2} - (t_1 - 1)^{3/2}\} \tag{3.12}$$

And for the third as:

$$p = 2(\frac{k}{varphi}b)^2\frac{dt}{dp} + p_2^* \tag{3.13}$$

where

$$p_2^* = p_2 + 2\frac{k}{\varphi}b(t_2)^{1/2} \tag{3.14}$$

where a depend of fracture height, the fracture Length R and the wellbore radius, b depend of the wellbore radius, the length of the pressurized interval, and k depend of the fluid loss coefficient, the time at shut-in, and the well bore radius.

Is important to notice that the behavior of both stages represented by eq 3.11 and eq 3.13 can be seen as the described as a straight line.

$$P_w - P \sim A(dPw/dt) + C \tag{3.15}$$

With A and C as parameters which depend on the problem geometry and on the material properties Cornet (2016).

On the other hand for the second stage there is no analytical model yet (Hayashi (1991)), nevertheless the pressure decline can be described in a qualitative fashion. Suppose the fracture is absent. Then the contribution of the maximum and minimum horizontal in situ compressive stresses to the hoop stress around the wellbore tested at the point corresponding to the fracture lip (where fracture meets well bore wall). To close the fracture at the fracture lip is necessary to the pressure acting in the fracture to become lower than the of the hoop stress due to horizontal stress and the fluid pressure. Meanwhile, the fracture tip closes when the pressure in the fracture decrease just below the minimum horizontal stress. Meaning that the lip of the fracture reaming open when the tip of the fracture is closed.

When the behavior of the three stage is put together it can be seen the first stage have a near linear performance, entering to the phase two this behavior is lost, so the end of the linearity of the transition between phase one and two provides an upper limit to minimun horizontal stress. The same analysis can be perform from stage two to three providing a lower limit.

A typical pressure record is shown on figure 3.6. It shows that an HF test includes at least three phases, the first two phases involve the development and the propagation of the hydraulic fracture together with fracture closure phases, the third phase involves the reopening of the fracture followed up by a fracture closure phase. This procedure provides two fracture closure and one fracture reopening, or three different estimates for the far field minimum principal stress magnitude. When possible, a second reopening phase is conducted so as to provide additional redundancy in the results.

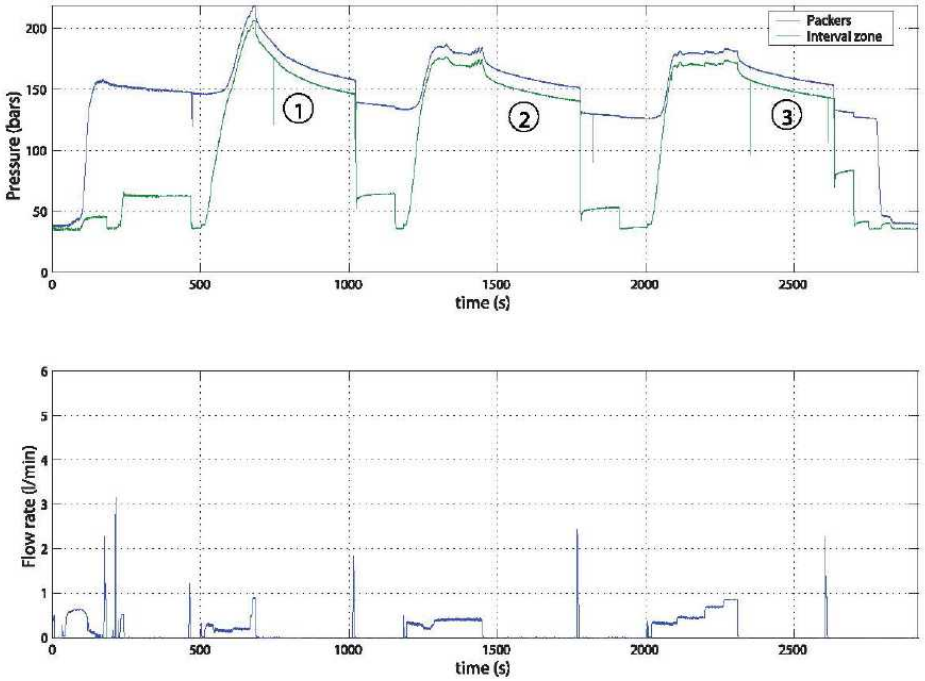


**Figure 3.6:** A Typical HF test. In the upper diagram. The blue curve is to the straddle packer, the green curve is to the interval pressure both as function time. The lower diagram represents the flow rate.

### 3.1.2 Interpretational Techniques

#### System Stiffness Approach

The behavior of the pressure respect to the time after the fracture is close depends on the interaction of two competing factor. One is the system stiffness (change in pressure over change in volume of the system) which is increase when fracture closed and contributes to an increase in the slope. the second factor is the leak-off rate decreases as the fracture closes and the flow path pinches off, contributing to a decrease in slope (Figure 3.7). Therefore, there is a combination of these two factor that would lead to a very sutil change in the slope of the pressure decay curve, making conventional analysis of p vs t inaccurate and very difficult to interpret closure pressure. The net result is unpredictable, nevertheless if the micro/minifrac is perform with flowback the change in slope must increase making the fracture closure pressure easier to identify. Raaen et al. (1991).

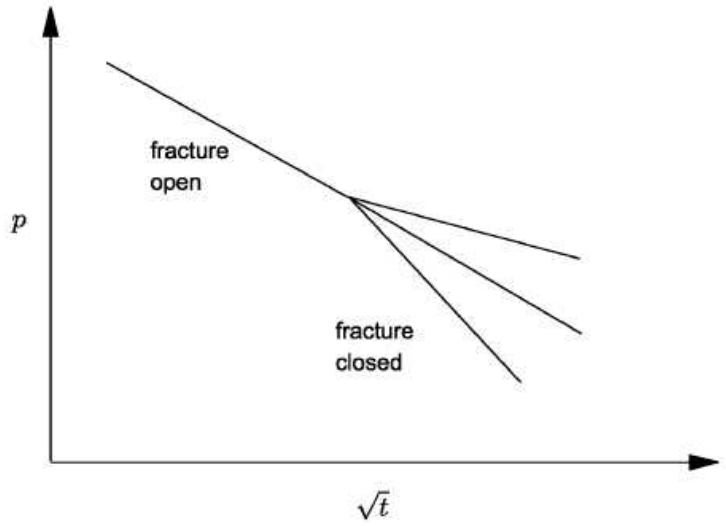


**Figure 3.7:** Behavior of the pressure respect to the square root of time. Different slopes correspond in which of the competing process (leakoff or stiffness) dominates the fracture.

The system stiffness approach is based in a simple conceptual model of what happens in a pump in- /flowback or a pump-in /shut-in test when the fracture closes. The fundamental statement of the model is that changes in the well pressure can be related to the mass of fluid entering or leaving the well/fracture system. Assuming the fluid to be a liquid, the density is nearly constant, and we may use the volume entering or leaving the system instead of the mass.

The pressure is then related to the change in system volume according to the simple equation

$$S = \frac{dP}{dV} \tag{3.16}$$

Note equation 3.16 is not normalized, therefore, the stiffness is dependent on the actual well configuration also the pressure P in principle may be either a downhole pressure or a surface pressure, related by the hydrostatic pressure due to the weight of the mud column. Eq 3.16 allows to predict how the pressure evolves with time, since we know how the system stiffness and the system volume change with time. Raaen et al. (1991).

During the micro/minifrac test the system volume may change according to two mechanisms, fluid flow into the formation and controlled flowback at the surface. If the rate of controlled surface flowback is considerably higher than the rate of leak-off into the formation, a direct measurement of the system stiffness (as a function of time) by plotting p versus flowback volume Vfb. On the other hand, if leak-off is the dominant factor, we have no volume control, and the interpretation must be based on the time development of p only, in other words, the stiffness approach is limited to a formation in which the leakoff rate is relatively low. Another assumption of this model is that the most of the leak-off will occur in the open fracture rather than in the open surface area of the well, this hypothesis is reasonable because in the case of an open hole minifrac test mudcake form by the drilling fluid will create an impermeable area in the hole, and by consequence most of the fluid loss will occur thru the fracture. Since most of the leak-off is through the fracture, the leak-off rate will change considerably as the fracture closes. Raaen et al. (1991)

The system stiffness is given by the stiffness of the fluid and the stiffness of the fracture. The fluid stiffness refers to the compression/decompression of the fluid volume in the well, since the fluid volume in the well is much bigger than the fluid in the fracture, is possible to get a good estimation of the fluid stiffness by knowing the fluid volume in the well and its compressibility.

The fracture contribution to the system stiffness is more complicated because it will depend on the fracture sizes. As stated before, during the closure of the fracture (stage 2, section 3.1.1) there is no analytic solution for the pressure decline and therefore the exact width of the fracture is unknown. Nevertheless, to get an order of magnitude of the fracture stiffness Raaen et al. (1991). assume and uniform width of the fracture (stage 1) and calculate the fracture stiffness using equation 3.16. With is assumption, it was found that the fracture stiffness is much lower than the fluid stiffness. Even when the result is reached for a specific case the conclusion of the different magnitude of the stiffness may be made for more general fracture shape. At the end is to expect a noticeable increase of the system stiffness when the fracture closed.

By plotting the pressure vs the system stiffness it can be easily determined at the change in slope the fracture closure pressure. In this case, the interpretation does not depend on a constant flowback rate, which is generally assumed in standard interpretations of flowback tests.

If volume data was not recorded during the treatment, the test must be analyzed based behavior of the pressure against the time. However, in Eq 3.16 is shown that if the system stiffness and the volume are known, the time development of pressure can be predicted. This offers an alternative way of performing a flowback test, using a constant choke. By having a constant choke during the flowback, the flowblack rate will decrease as the system pressure decreases. Nonetheless, there is a relation between the pressure drop across the choke and the flow rate. By assuming a pressure dependence of stiffness, we may then predict pressure versus time, and hence deduce optimal ways of plotting the data. (Raaen et al. (1991).

It is possible to use the stiffness method approach in the interpretation of a pump-in/shut-in test, nevertheless is necessary to have low permeation of fluid through the fracture, which implies a tight mud cake or low permeability in the formation Raaen et al. (1991) determinate that with a plot of pressure differentiated with respect to the square root of time versus the square root of time the same features observed during the pump-in/flowback test appears, allowing the interpretation of the fracture closure pressure when an increase on the system stiffness is observed.

Is important to highlight due to the complexities of the fracture closure process (section 3.1.1)the stiffness approach provides a simple and obviously more imprecise approach. Considering that is useful to distinguish between mechanical and hydraulical closure, where mechanical closure occurs when asperities of the two fracture faces start to contact (second stage) (i.e. when the stress on the fracture faces starts to increase above the fluid pressure), while hydraulical closure occurs when the fracture stops being conductive (third stage). Mechanical closure is considered to represent the in situ stress. The pressure at mechanical closure must be greater than (or at least equal to) the pressure at hydraulical closure.

### G function

One important method that minimizes ambiguity and provides useful in-situ stress and leak-off information is the G-function analysis. It is derived so that the cumulative fluid leaked-off volume from the fracture after shut-in is linearly proportional to the G-function. In other words, at a G-time =4, twice as much fluid has leaked-off after shut-in as at G-time=2. The G-function is a dimensionless time function that relates shut-in time to total pumping time. This process uses derivative curves to identify leak-off mechanisms and fracture closure point through the characteristic shapes of the curves. The G-function plot features a pressure and semi log derivative of pressure vs. G-time curve. In many cases, the expected signature of the semi log curve is a straight line that passes through the origin, representing normal fluid leak-off behavior. Fracture closure point is identified at the point when the G-function semi-log derivative curve starts to deviate from its straight tangent line in a normal leak-off (most ideal) case  Tangent Method.

This technique was introduced by Nolte (1979), and has been widely used in the industry. G-function does not assume a single planar fracture and will show the effects of multiple fracture planes propagating against different closure stresses. One important assumption in G-function derivation is that the fluid pressure is constant during shut-in. Clearly, fluid pressure is not constant and decreases over time after shut-in. But during early shut-in period, it is approximately valid to assume that the fracture pressure is constant. The normal leak-off model is applied to the sole case of perfectly linear pressure decay on the P vs. G plot. However, deviation from this ideal behavior is generally expected. The other pressure fall-off scenarios are pressure dependent leak-off, fracture height extension and transverse storage, fracture tip extension. The G-function curves for each of these scenarios display a different signature; therefore, analysis and interpretation for each case are also handled differently.

Derivation
The basic assumptions for the applicability of the analysis are that the fracture:

1. has essentially constant height.
2. propagate through a quasi.-elastic formation with negligible slip of bedding planes.
3. was created by a constant injection rate of a power-law fluid into two symmetric wings.
4. propagates continuously during pumping and propagation stops when pumping stops.
5. closes freely without significant interference from proppant.

Nolte continues the work of Nordgren who states that the equation for flow down a fracture can be represented as

$$-\frac{\partial Q(z,t)}{\partial z} = \lambda(z,t) + \frac{\partial A(z,t)}{\partial t} \tag{3.17}$$

This equation denote that the gradient of a flow rate is equal to the rate fluid lost to the formation, per unit of length, plus the time rate fluid storage due to cross-sectional area change (Nolte (1979)). Nolte assumes as well the fluid loss relationship ($\lambda$) and the cross section area are given by:

$$\lambda = \frac{2CH_p}{\sqrt{t-\tau(z)}} \tag{3.18}$$

$$A = \frac{\pi}{4}wH = \frac{\pi H^2}{2E'}P \tag{3.19}$$

Where, C is the fluid loss coefficient, $H_p$ is the height over the fracture where fluid loss occurs, $\tau$ is the time the fracture was created at point z. H is the fracture height, w is the maximum fracture width at z. P is the pressure of the formation a E is the effective plane-strain modulus across the fracture height.

By combaning equations 3.17 to 3.19 results in

$$-\frac{\partial Q}{\partial Z} = \frac{2CH_p}{\sqrt{t-\tau}} + \frac{\pi}{2}\frac{H^2}{E'}\frac{\partial p}{\partial t} \tag{3.20}$$

And then integrating equation 3.20 yields to:

$$-Q(L) + Q(0) = 2CH_p \int_0^L \frac{dz}{\sqrt{t-\tau(z)}} + \frac{\pi}{2}\frac{H^2}{E'}\int_0^L \frac{\partial p}{\partial t} dz \tag{3.21}$$

Further assumption are required, if the fracture is shut-in and free extension of the tip after the shut-in has ceased (Q(0)= Q(L) =0) and substituting this assumption in equation 5 and replacing the integrals for the average value of the function over the length of the fracture Nolte (1986).

$$0 = \frac{2CH_pL}{\sqrt{t_0}} f(t) + \frac{\pi}{2}\frac{H^2}{E'} L\frac{\partial \bar{p}}{\partial t} \tag{3.22}$$

where

$$f(t) = \frac{\sqrt{t_0}}{L}\int_0^L \frac{dz}{\sqrt{t-\tau(z)}} \tag{3.23}$$

$$\bar{P} = \frac{1}{L}\int_0^L p dz = \beta_s P \tag{3.24}$$

In equation 3.22 $T_o$ correspond to the injection time prior to shut-in and in equation 3.24 P is the wellbore pressure. $\beta_s$) is defined as the ratio of the average pressure to the wellbore pressure. By combining equation 3.22 3.23 and 3.24

$$\frac{dP}{dt} = -\frac{4}{\pi}\frac{CH_pE'}{H^2\beta_s\sqrt{t_0}} f(t) \tag{3.25}$$

The pressure decline function, f, in equation 3.23 can be evaluated by an upper and lower limit, these limits comes from the time the fracture creation $\tau(z)$ and require the assumptions that the height, injection rate and injection fluid are constant and that the fracture propagates continuously during pumping.

The lower bound on the rate of extension is for the fluid-loss dominated case and assumes that the first term on the right hand side of equation 3.17 dominates the behavior of the pressure decline function making the fluid storage term neglected. On the other hand the upper bound assumes minimal fluid loss making the term of $\lambda$ on equation 3.17 neglected Nolte (1986).

$$\begin{aligned} f_{upper} &= 2(\sqrt{1+\Delta t/t_0} - \sqrt{\Delta t/t_0} \\ f_{lower} &= \sin[(1-\Delta t/t_0)^{1/2}]^{-1} \end{aligned} \tag{3.26}$$

Where, $t_0$ at which the shit in occurs, delta t is the time since the shut-in, $\Delta t/t_o$ is the dimensionless shut-in time in terms of the pump-in. Nevertheless, Nolte (1986) establish that both bound are fairly close to each other and usually differ by less than a 10%, as a result any of the bound can be used to solve the equation 3.25 without compromising the accuracy of the solution. In follow , $\Delta t/t_0$ will be refer as $t_d$.

The pressure difference between two shut-in time can be found after integrating the equation 3.25 between two times and can be express as

$$\Delta P(\delta_0, \delta) = \frac{C H_p E' \sqrt{t_o}}{H^2 \beta_s} G(\delta, \delta_0) \tag{3.27}$$

for which

$$\begin{aligned} \delta &= \Delta t/t_0 \\ \Delta P(\delta_0, \delta) &= P(\delta_0) - P(\delta) \\ G(\delta, \delta_0) &= \frac{4}{\pi}[g(\delta) - g(\delta_0) \end{aligned} \tag{3.28}$$

and the upper and lower bounds of the function g are:

$$\begin{aligned} g_{upper} &= \frac{4}{3}[1+\delta)^{1.5} - \delta^{1.5}] \\ g_{lower} &= \frac{4}{\pi} \sin^{-1}(1+\delta)^{-0.5} + \delta^{0.5} \end{aligned} \tag{3.29}$$

Castillo (1987)rewrite the equation 3.27 in terms of C is the leakoff coefficient, $f_p$ is the ratio of permeable area to gross area and $c_f$ is fracture's compliance for width.

$$\Delta P(\Delta t*, \Delta t) = \frac{\pi C f_p \sqrt{t_p}}{2 c_f} G(t_D, t*_D) \tag{3.30}$$

By selecting a dimensionless time ($t_D$) earlier than fracture closure and plotting G function versus $t_D$ on log-log coordinates. The same reference time is use to plot $\Delta P$ against $\Delta t$. A curve match can be obtained by overlying the curves, aligning the x axes so that $\Delta t$ correspond to $t_D$ and shifting along the y axes. Once the match is achieved, a match point is selected and the Nolte match pressure (P*) is computed from $\Delta P/G$. the match is equivalent to:

$$P^* = \frac{\pi C f_p \sqrt{t_p}}{2 c_f} \tag{3.31}$$

If the fracture compliance is fixed, the leakoff coefficient can be estimated from Equation 3.31. Then Castillo proposed a new plot by realizing that Equation 3.30 is a linear equation. Substituting Equation 3.31 into Equation 3.30, and selecting a reference time of $\Delta t^* = 0$ results in:

$$P(\Delta t) = P * G(t_D, 0) + P(\Delta t* = 0) \tag{3.32}$$

This equation is in the familiar form of $y = mx + b$. Therefore, a plot of decline pressure against should result in a straight line during the closure period with slope equal to P* and y-intercept equal to a theoretical pressure at shut-in. The closure period is recognized by linearity; deviation from linearity identifies the closure pressure. From this single plot, then, all of the pressure parameters ( Pc, P*, ISIP) required in the analysis calculations are inferred. Interpretation of the G-Function plot is enhanced by differentiating Equation 3.32 to give

$$\frac{dP}{dG} = P* \tag{3.33}$$

A graph of $dP/dG$ against t (referred to as the G-Function derivative plot) should provide a horizontal line during the closure period with a constant y axis value of P*. The derivative, $dP/dG$, may be computed by using linear regression on a small number of data points (e.g. 5); the t value that corresponds to $dP/dG$ is a time average of the points used. Fracture Closure pressure can be easily identify as well by the departure of the semi-log derivative of pressure with respect to G-function $(Gdp/dG)$ from the stright line through the origin (Castillo (1987), Barree et al. (2007),Michael J. Economides (2007)) . In the following image is show a semi log plot of the pressure and the derivatives of pressure against the G function and it can be clearly identify the fracture closure pressure

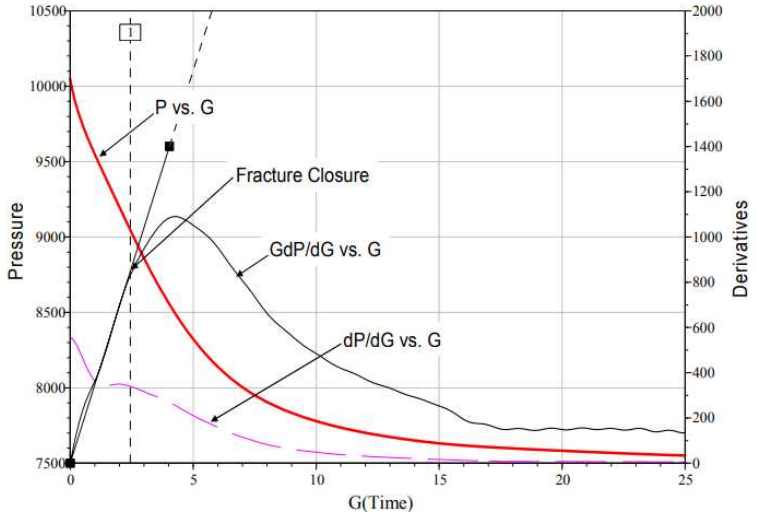


**Figure 3.8:** Normal leak-off G function plot.

Chapter 4

# Methodology

As stated before (Chapter 1) the idea of this work is to understand fracture initialization around the borehole having in consideration plastic material behavior. In order to accomplish this task, it was implemented a finite element analysis.

## 4.1 Geometry

First of all, a geometry of the model has to be established. Since the objective of the analysis is to perform the simulations in a typical operational environment for the oilfield industry and specifically for a fracture operation. The model consists in a cube of 5 meters length, high and deep, buried at 3000 m deep in the center of the cube it was set a vertical hole that will simulate the borehole. This borehole has 0.3m radio, simulating a typical hole section, the arista size of 5 meters was choose in order to be big enough to avoid edge effect on interest section (around the borehole) figure 4.1.

In order to have results as accurate as possible is important to have elements as small as possible in the interest zone. Nevertheless, a large number of elements will increase dramatically the computer power and time required to achieve a solution in each run. Thus, is important to have a balance between the accuracy required to have reliable results and optimize the amount of time of each run. Since the most sensitive area is the first few centimeters around the borehole in this zone the mesh size is smaller, and the cell size is increasing as the distance from the center of the cube increase figure 4.2.

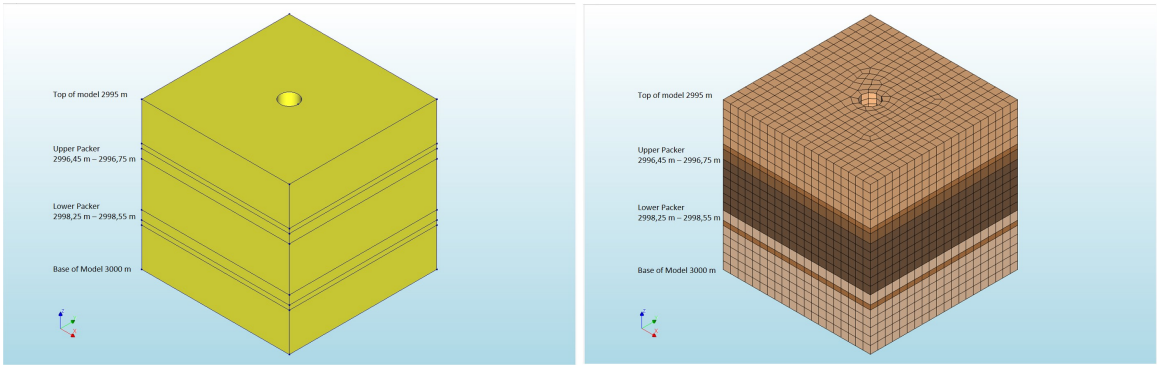


**Figure 4.1:** Geometry and mesh of the model showing the subdivision of it on, Overburden, Underburden, Upper and Lower Packer, Zone between the packers and zone of high resolution above and below the packers.

One important part of this project was to asses the behavior and influence of the packers during a micro-frac operation. In order to determine the stress and strain distribution not only in the zone between the packers but also the packers zone and it surrounding (above and below of the packer). In order to have a good resolution of the results the model was divided in zones according with the previous description. In the same way, since the stress concentration and rock deformation is concentrated in the surrounding of the borehole, another areas were also defined in order to set an appropriate cell size. The closet zone is from the wellbore wall until 0.1m inside the formation, this zone will have a cell size of 0.02m. 0.4m away from the center of the model until 0.7m the cell size was set to 0.05m, in the same way from 0.7m to 1.2m the cell size was increased to 0.1m and finally for 1.2m to the edge of the model at 2.5m the cell size will increase progressively until 0.25m. Having this smooth change in cell sizes will allow the numerical model to have an accurate solution in the interest zone as well as optimizing the number of cell in the whole model. in the end the final geometry has a total of 275.521 elements.

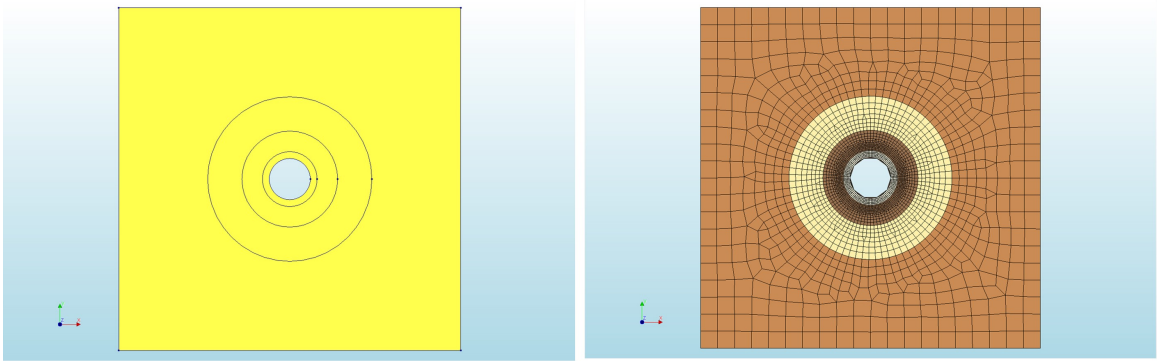

**Figure 4.2:** Geometry and Mesh: plant view the the mesh, showing small elements near the wellbore and the progressive increment towards the edge.

## 4.2 Rock Properties and In situ Stresses

The rock properties used for this simulation where assigned having in mind typical reservoir properties. Nevertheless, the objective of the work was not to simulate a particular field but to develop an understating of the behavior of plastic rocks. In that way the implemented rock

properties are specified on the table below (Table 4.1). One of the limitations of the finite element software used to run the simulation was the inability of allowing couple modelling, in other words, there is no interaction between the fluid inside the borehole and the fluid inside the rock, however this can very often be the situation in a borehole environment, if the permeability of the rock is very low or if the effectiveness of the mud cake build during the drilling process is very high, can lead to a situation of no interaction between fluid in the wellbore and the rock.

Once the geometry and the rock properties have been establish, the next stage is to set the stress state. Since the model is only 5 meter high is necessary to apply at the top of the model (@ 2995 m) a pressure equivalent to the overburden pressure. Assuming an overburden density of 2150kg/m3 the overburden pressure at the top of the model was determine at 67.5 Mpa. Regarding the horizontal stress, for the comparison between the analytical and numerical case, two settings were applied, the first one assuming horizontal stress isotropy as a 0.75 of the vertical stress, and the second was to set the maximum horizontal stress and minimum horizontals stress as a fraction of the vertical stress, 0.85 and 0.75 respectively, the maximum stress azimuth is parallel to the X axis. Another important factor is the pore pressure, which was to have a normal pressure in the whole model.

## 4.3 Analytical vs Numerical Solution

The next stage is to test the numerical solution and compare it with analytical calculation in order to verify the parameters are set in a proper manner and as well as build confidence in the accuracy of the geometry and mesh proposed. The simplest way to accomplish that is by performing a linear elastic run of the model for different pressure inside the wellbore. Some rock properties has to be define previous the linear elastic model initialization as Young modulus, Poison ratio, and Friction angle; these properties are specified in the table below (4.1). The chosen failure criteria is Mohr Coulomb.

| **Properties** | **Value** |
|---|---|
| Saturated Density | 2300 $kg/m^3$ |
| Young's Modulus | 5 $GPa$ |
| Poisson's Ratio | 0.3 |
| Cohesion | 2 $MPa$ |
| Friction angle | $30^\circ$ |

**Table 4.1:** Rock Properties.

The analytical response, the stress around the borehole was calculated using the Kirsh equation, which describe the behavior of the axial, tangential and radial stress depending of the distance of the observation point and the borehole radio for elastic behavior. In the case of vertical hole and assuming as described on the proposed model that the principal stresses correspond with the vertical and horizontal stresses. The stresses around the borehole can be expressed as demonstrated by Fjaer et al. (2008).

$$
\begin{aligned}
\sigma_r &= \frac{\sigma_H + \sigma_h}{2}(1 - \frac{R_w^2}{r^2}) + \frac{\sigma_H - \sigma_h}{2}(1 + 3\frac{R_w^4}{r^4} - 4\frac{R_w^2}{r^2})\cos 2\theta + p_w\frac{R_w^2}{r^2} \\
\sigma_\theta &= \frac{\sigma_H + \sigma_h}{2}(1 + \frac{R_w^2}{r^2}) - \frac{\sigma_H - \sigma_h}{2}(1 + 3\frac{R_w^4}{r^4})\cos 2\theta - p_w\frac{R_w^2}{r^2} \\
\sigma_z &= \sigma_v - 2\nu_{fr}(\sigma_H - \sigma_h)\frac{R_w^2}{r^2}\cos 2\theta
\end{aligned}
\tag{4.1}
$$

Where $\sigma_H$ represents the maximum horizontal stress, $\sigma_h$ minimum horizontal stress, $\sigma_V$ vertical stress, $\nu_{fr}$ the framework poison ration, $p_w$ pressure in the wellbore, $R_w$ wellbore radio, and $\theta$ the azimuth angle relative to the direction of the maximum horizontal stress.

From equations 4.1 it can be seen that at the wellbore wall the tangential stress will have critical values at $\theta = 0$ and $\theta = 90$, at this points is where the shear failure and the tensile fracture will initiate. Therefore, those are the point in which the analysis will focus.

Now, among all the presented output on the finite element software used to develop this project there exists the option to have the stress in X, Y and Z direction for each point. According to (Bower (2009)) the conversion between Cartesian to a Polar-Cylindrical tensor is given by simplifying the expression for $\theta$=0 one can find that the radial stress correspond to the Sxx (stress in X direction) and the tangential stress to Syy (stress in Y direction). Thus, for $\theta = 90$ the radial stress is equivalent to Syy and axial stress to Sxx. Note, for values of $\theta$ between 0 and 90 the solution is not that intituive, nonetheless, the calculation of the tangential stress could be easily calculated by solving the equation above. However, by limitation on the exporting tool on the software and more important, since the critical values are at $\theta$ 0 and 90 for the shear failure and tensile failure initiation in enough by having the values along this angles. For both cases the axial stress correspond to Szz

$$
\begin{bmatrix} S_{xx} & S_{xy} & S_{xz} \\ S_{yx} & S_{yy} & S_{yz} \\ S_{zx} & S_{zy} & S_{zz} \end{bmatrix} = \begin{bmatrix} \cos\theta & -\sin\theta & 0 \\ \sin\theta & \cos\theta & 0 \\ 0 & 0 & 1 \end{bmatrix} \begin{bmatrix} S_{rr} & S_{r\theta} & S_{rz} \\ \S_{\theta r} & S_{\theta\theta} & S_{\theta z} \\ S_{zr} & S_{z\theta} & S_{zz} \end{bmatrix} \begin{bmatrix} \cos\theta & \sin\theta & 0 \\ -\sin\theta & \cos\theta & 0 \\ 0 & 0 & 1 \end{bmatrix} \tag{4.2}
$$

$$
\begin{bmatrix} S_{rr} & S_{r\theta} & S_{rz} \\ \S_{\theta r} & S_{\theta\theta} & S_{\theta z} \\ S_{zr} & S_{z\theta} & S_{zz} \end{bmatrix} = \begin{bmatrix} \cos\theta & \sin\theta & 0 \\ -\sin\theta & \cos\theta & 0 \\ 0 & 0 & 1 \end{bmatrix} \begin{bmatrix} S_{xx} & S_{xy} & S_{xz} \\ \S_{yx} & S_{yy} & S_{yz} \\ S_{zx} & S_{zy} & S_{zz} \end{bmatrix} \begin{bmatrix} \cos\theta & -\sin\theta & 0 \\ \sin\theta & \cos\theta & 0 \\ 0 & 0 & 1 \end{bmatrix} \tag{4.3}
$$

On figure 4.3 are shown the comparison between numerical and the analytical solution for the linear elastic case for different wellbore pressure (emulating the mud weight) as well as for different values of $\theta$ and stress anisotropy. The numerical data is represented by the continuous line, meanwhile the analytical calculation is plotted as a points. The curves match as expected for all the different simulation performed. One can note on the neighborhood of the wellbore the change rate (gradient) of the stresses is high as the observation point is further apart of the wellbore wall the stress magnitude reach the far field stress field. The implication on the numerical model of this high gradient will be discussed in more detail in further chapter.

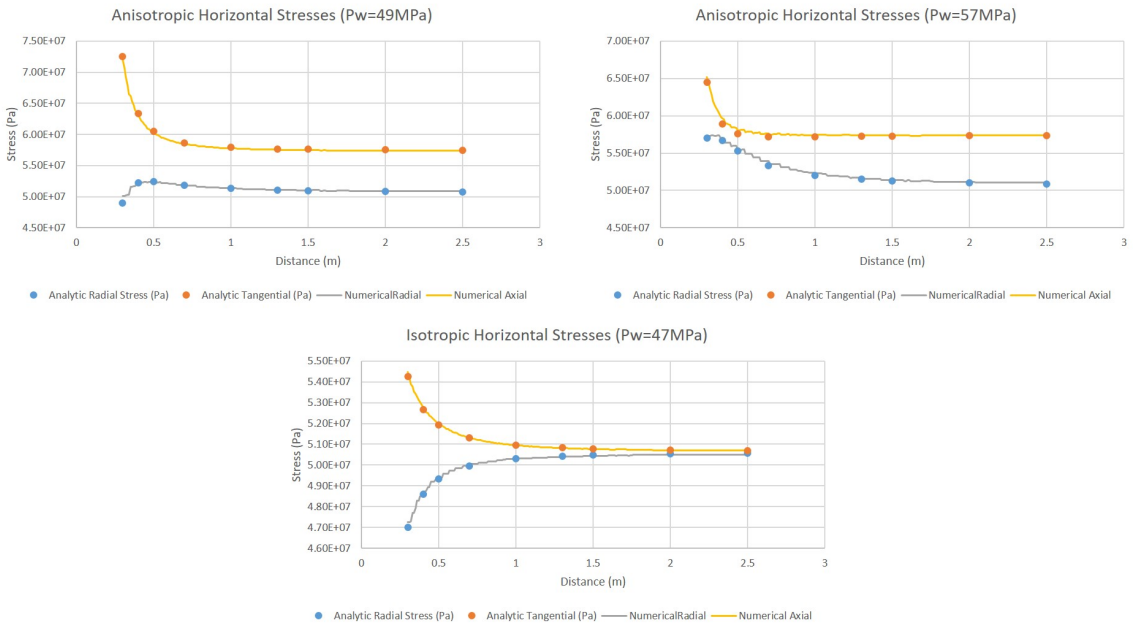


**Figure 4.3:** Comparison between analytical and numerical case for different for isotropic and anisotropic case with different Pw.

## 4.4 Plasticity Model

Once the parameters have been checked with the comparison between the analytical and numerical case, is possible to move on towards the plasticity modelling. The plasticity criteria to be used is the Mohr coulomb criteria. In order to use this criteria additional parameters have to be defined besides the one used for the linear elastic as the dilatancy angle. During the upcoming simulations the model will be set as a associated plasticity model (see section 2.2.2) which means that dilatancy angle and the friction angle have the same value.

On the other hand, the main focus will be the hardening behavior of the rock, thus, the hardening rule will be updated in each run in order to quantify the behavior of the stress and strain distribution due to the plastic behavior of the rock .

Generally the hardening parameter will depend not only of the current plastic strain but on the plastic strain history as well. This can lead to very complex theories but Vermeer and De Borst (1984) propose to avoid this inconvenient by claiming that the plastic strain history can also be registered on the hardening parameter. Numerically the hardening factor for the Mohr Coulomb criteria according to Hill (1950) the can be expressed as:

$$\bar{\varepsilon^p} = \int \sqrt{\frac{2}{3}(\dot{\varepsilon_1^p}\dot{\varepsilon_1^p} + \dot{\varepsilon_2^p}\dot{\varepsilon_2^p} + \dot{\varepsilon_3^p}\dot{\varepsilon_3^p})}dt \tag{4.4}$$

The dot above a symbol implies the material time derivative which controls the sequence of the loading process. Since this kind of loading and viscous effects are out of the scope of the project the hardening parameter can be simplified to:

$$\bar{\varepsilon^p} = \sqrt{\frac{2}{3}((\varepsilon_1^p)^2 + (\varepsilon_2^p)^2 + (\varepsilon_3^p)^2} \tag{4.5}$$

## 4.5 Output Display

After the simulation is perform the output display plays an important part on the analysis to come. On the finite element analysis software there are several ways to display stress and strains. For instance, on the stresses are available among others the normal stresses together with the shear stress with which the whole stress tensor is represented as well as the principal stress.

The normal stress and shear stress are perpendicular to each other, thus, for every azimuth there are a stress vector with normal and shear components. Nevertheless, there is a space on which the shear component is zero, making the normal component equal to the whole stress vector. The stress at this direction are called principal stresses. On the following figure are shown the normal stresses and the principal stresses around the borehole for a given mud weight. As stated before, they represents the same state of stresses but in different ways. Since the main focus is to study the behavior at the borehole wall and as shown before on the equation XX under specific circumstances there is a direct relation between the normal stress and the hoop stresses (tangential, radial and axial stress). Having this under consideration the following result will be shown as a normal stress (Sxx, Syy, Szz) because along the specified direction of $\theta$ = 0 or $\theta$ =90 is simple to get the hoop stresses and in further calculation performed stress invariant calculation and /or compare the stress stated with the failure envelop.

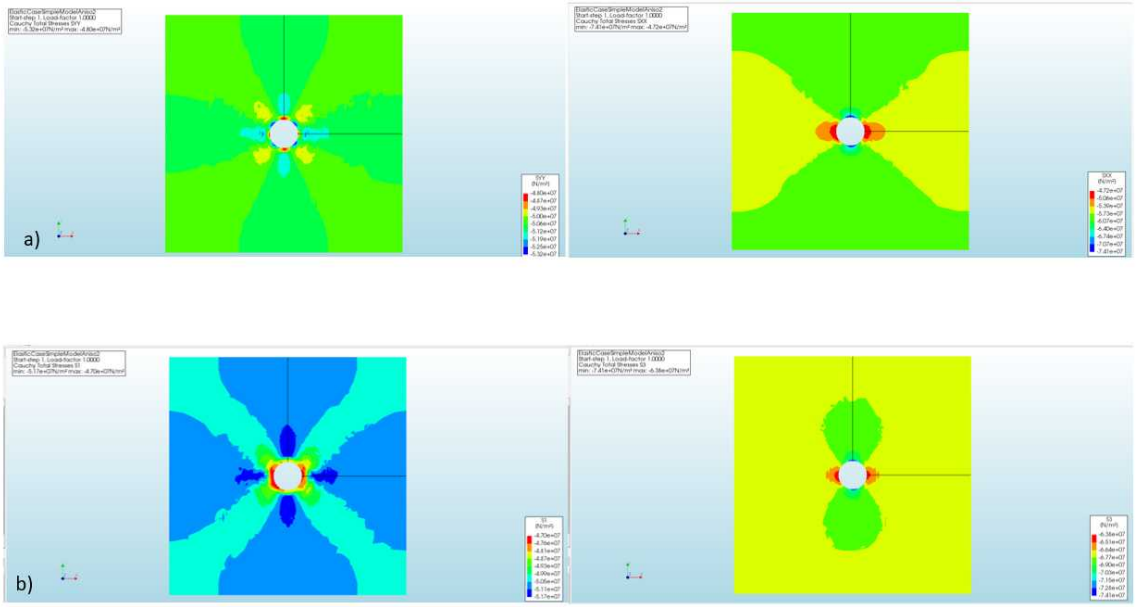


**Figure 4.4:** a) Component X and Y of the stress tensor. b)Principal Stresses S1 and S3

In the case of strains, is easier to visualize the extend of the deformation by analyzing the volumetric plastic strain, which is just the sum of the three principal components of the strain tensor. However, due to the calculation of the hardening parameter is expressed in term of three principal components of the strain tensor sometimes it will be useful to display the strains in this way.

Chapter 5

# Results and Analysis

This chapter presents the results obtained for each stage of the project with their respective analysis. Firstly, the linear elastic case is presented for different injection stage (increments of pressure in the wellbore) with the respective Mohr circle present for each stage. Then by the plasticity model using the Mohr-Coulomb criteria with different hardening rules. Finally, the effect of the packer in the formation above and below it.

## 5.1 Linear elastic: Case 1

The first run of the model was performed for a linear elastic material. This case had horizontal stress isotropy. The horizontal stresses are equivalent to 0.75 of the overburden stress. On figure 5.1a shows stress distribution on X component of the stress tensor, in this example the pressure inside the borehole is 47MPa. Due to the horizontal stress isotropy, the component Y (figure 5.1b) shows exactly the same behavior, but rotated 90 degrees. Because of that fact, the shear failure and the stress initialization have no preferential azimuth of occurrence making the rock fairly stable.

Through analytical calculations it was determined the pressure inside the borehole (mud weight) required to have an effective tangential stress equal to zero (tensile failuren assuming zero tensile strength) as well as the pressure to generate shear failure (breakout). The necessary pressure inside the hole necessary to reach the breakout condition was 41.5MPa and for tensile failure initiation that condition is equivalent to 71.9MPa. The analytical calculation correlates with the numerical solution as expected, showing the transition of the stresses nearby the wellbore and the far field stresses. Nevertheless, it was noticed that when the initialization values of the simulation are close to the failure point, the numerical iteration tend to be unstable and therefore the solution of the system of equation diverge. Having this in consideration the initial borehole pressure of each of the following case it is on the stable zone and the pressure will increase progressively (a few megapascals on each iteration) until simulate a Micro/minifrac operation.

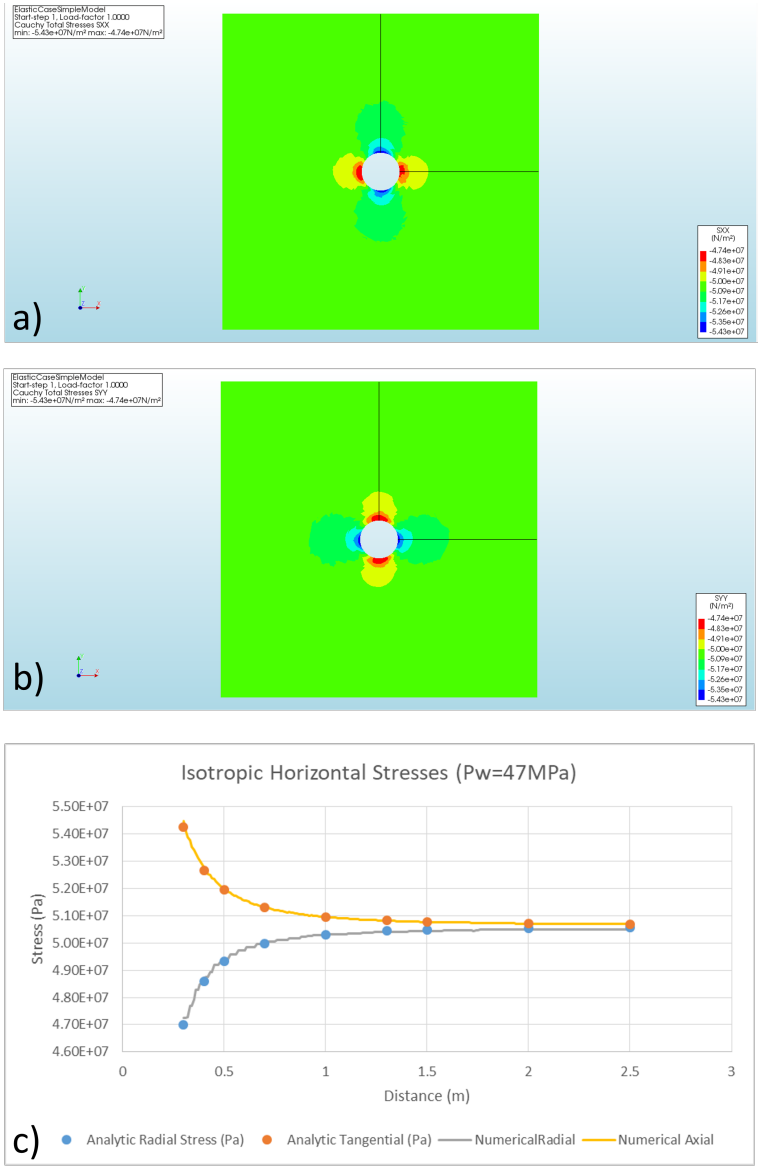


**Figure 5.1:** Horizontal Stress Isotropy @2997.5m, Pw=47MPa. a) component X of the stress tensor. b) component Y of the stress tensor. c)comparison of analytical and numerical solution

The next simulation was run with the same rock properties and failure envelop but in this case, a horizontal stress anisotropy was introduced. $\sigma_H = 0.85\sigma_V$ and $\sigma_h = 0.75\sigma_V$, the azimuth of the maximum horizontal stress is parallel to the X axis. As establish on the previous chapter the critical points are for $= 0°$ and $= 90°$. Following the same procedure has in the horizontal stress isotropy, the analytical calculation was performed and the pressure to initiate shear and tensile failure are 48.2MPa and 65.1Mpa respectively. The initial wellbore pressure was set to 49Mpa (stable zone) to avoid numerical problems and as it was done in the previous case the pressure was increased in each injection stage. On the figure 5.2 a and b shows the X and Y component of the stress tensor when the pressure inside the well is 57MPa. Comparing the numerical and analytical solution. The corretlation is as good as in the isotropic case as can be seen in 5.2 c and d .

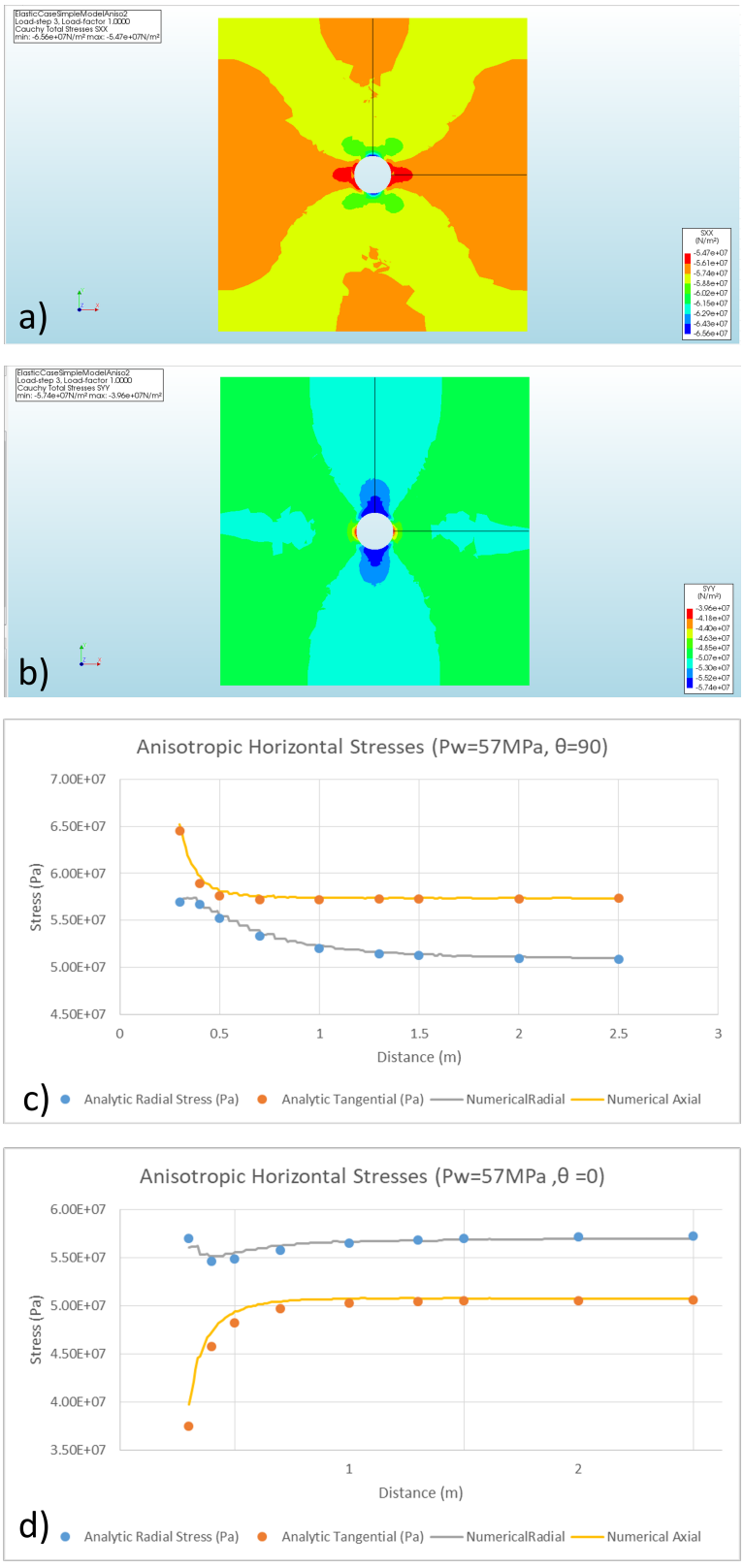


**Figure 5.2:** Horizontal Stress Anisotropy @2997.5m, Pw=49MPa. a) component X of the stress tensor. b) component Y of the stress tensor. c)comparison of analytical and numerical solution $\theta = 90$. d)comparison of analytical and numerical solution $\theta = 0$.

The importance to perform the linear elastic simulation lies as quality control of the input parameters as well as the finite element software. Once the material reaches the plasticity, the

behavior of stress is not as simple as in the linear elastic rocks, therefore in case of any discrepancy between the numerical and analytical model was identified at this stage; several inputs, as well as the geometry and mesh sizes would had to be reviewed in order to warranty the quality of the upcoming results.

## 5.2 Plastic material with hardening rule: Case 2

The next stage is to introduce the plastic behavior of the material. As discussed in chapter 2, the rock ideally could be classified as elastic-plastic with strain hardening, elastic-perfectly plastic, and rigid-perfectly plastic. The rock subject to the model will have a strain hardening behavior rule until a threshold in which the strength of the rock remain constant regardless of the strain showing a perfectly plastic behavior. Different hardening rules will be applied to the material in order to determine the behavior of stresses and strains.

As shown in the previous chapter the initial cohesion of the rock is 2MPa. When the rock start deforms in a plastic way this cohesion has to be updated using the relationship between deformations and hardening parameter, finally knowing the hardening rule (Table 5.1)for each simulation a new cohesion and therefore failure envelop can be calculated for each injection stage.

In the literature there are many compressive stress tests that can be used to show the behavior of a rock once touch the yield point (Cheatham Jr et al. (1967), Risnes et al. (1998)). The first simulation will be realized with a hardening rule as follows.

| **Hardening factor** | $S_0$ **plastic (MPa)** |
|---|---|
| 0 | 2 |
| 0.01 | 3 |
| 0.1 | 3 |

**Table 5.1:** Hardening rule for case 1 ($S_0$ plastic until 3MPa)

The figure 5.3 shows the stress distribution along the model on a horizontal plane at 2997.5 m deep (center of the model) with 52MPa of pressure inside the well; the black lines represent the probes used for extracting the data from the model. As shown in the figure 5.3c the stress state of the rock at the wellbore wall is the safe zone. As expected if the stress state is below the failure criteria, all the deformation at this moment are elastic (zero plastic deformation)(figure 3d). As soon as the analytical solution touches the Mohr-Coulomb criteria the numerical model begins to experience plastic deformation.It is important to note that the analytical solution was only performed for the linear elastic case, therefore for further comparison between analytical and numerical solution it will be based on the linear elastic versus plastic behavior for the same borehole pressure.

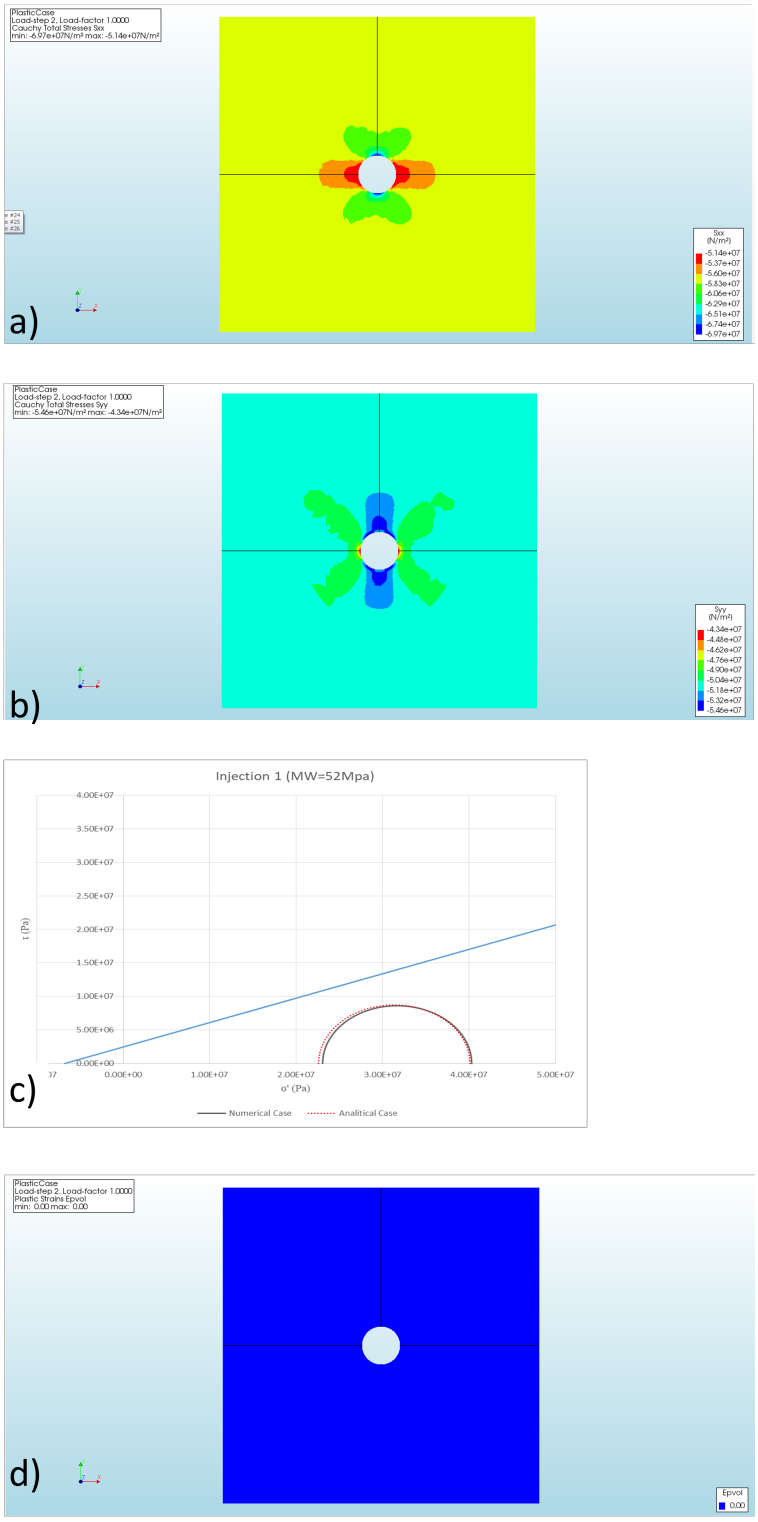


**Figure 5.3:** Case 2: Plastic Material. Horizontal Stress Anisotropy @2997.5m, Pw=52MPa. a) component X of the stress tensor. b) component Y of the stress tensor. c)comparison of analytical and numerical solution $\theta = 90$. d)Volumetric plastic deformation

In the following tables are shown the analytical and numerical solution for different injection stages (Table 5.2) and the strain on X, Y and Z components together with the calculation of the hardening parameter and the Cohesion for the plastic material ($S_0$ plastic) (Table 5.3), all these values are for $\theta = 0$ due to this point will be in which the fracture initiation will occur. The

following image (figure 4) shows the same arrange of images as before, the difference is that in this injection stage the wellbore pressure is 64Mpa.

| | **Analytic Radial Stress (Pa)** | **Analytic Tangential Stress (Pa)** | **Analytic Tangential Stress (Pa)** | **Analytic Tangential Stress (Pa)** |
|---|---|---|---|---|
| Initial Case | 4.90E+07 | 7.25E+07 | 4.96E+07 | 7.25E+07 |
| Injection1 | 5.20E+07 | 6.95E+07 | 5.25E+07 | 6.97E+07 |
| Injection2 | 5.40E+07 | 4.05E+07 | 5.42E+07 | 4.37E+07 |
| Injection3 | 5.70E+07 | 3.75E+07 | 5.67E+07 | 4.30E+07 |
| Injection4 | 6.20E+07 | 3.25E+07 | 6.16E+07 | 4.20E+07 |
| Injection5 | 6.40E+07 | 3.05E+07 | 6.34E+07 | 4.26E+07 |

**Table 5.2:** Analytical and numerical solution for different injection stages

| | **EpXX** | **EpYY** | **EpZZ** | **Hardening factor** | $S_0$ **plastic (MPa)** |
|---|---|---|---|---|---|
| Injection 2 | 3.18E-07 | 3.89E-04 | -1.91E-04 | 4.33E-04 | 2.04E+06 |
| Injection 3 | 1.22E-06 | 1.24E-03 | -6.10E-04 | 1.38E-03 | 2.14E+06 |
| Injection 4 | 2.61E-06 | 2.64E-03 | -1.30E-03 | 2.94E-03 | 2.29E+06 |
| Injection 5 | -8.61E-04 | 4.40E-03 | -1.29E-03 | 4.67E-03 | 2.47E+06 |

**Table 5.3:** Strain components X, Y and Z, hardening parameter and $S_0$ plastic

As it can be appreciated in figure 5.4 a and b shows a stress distribution along the model for the horizontal plane located at 29975.5m. The figure 5.4c presents the Mohr circle together with the failure envelope for both analytical an numerical solution; from now every in case every that reaches plastic deformation, two failure envelope will be shown, one correspond to the state before the plastic hardening (blue line) and the other (purple) correspond to the state after the injection stage. I this case specifically the mud weight was set to be 64 MPa. Is important to notice that the final stress state of the rock match almost spot on with the new failure envelop, as well we can observe through the comparison between both Mohr circle the analytic (linear elastic) case is really close to fulfilling the tensile failure criteria, meanwhile the numerical (plastic) has built an stress cage which prevents that Mohr circle grows and reach the null or negative values. Also important is to notice in figure 5.4d the zone in which the rock has withstood plastic deformation is confined only to 22 cm away from the wellbore wall, beyond that plastic zone the material still behave in a linear elastic manner.

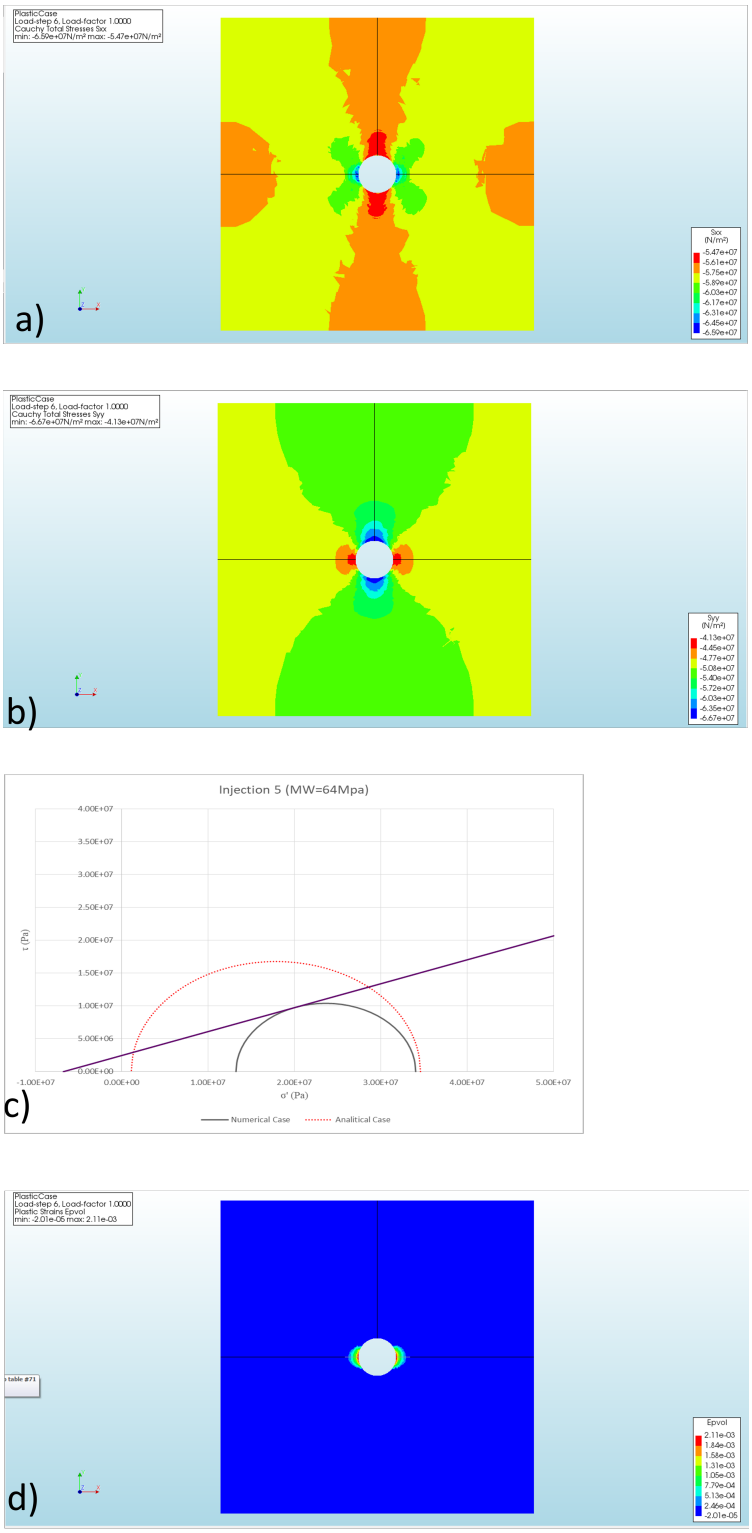


**Figure 5.4:** Case 2: Plastic Material. Horizontal Stress Anisotropy @2997.5m, Pw=64MPa. $S_0$plastic = 3Mpa. a) component X of the stress tensor. b) component Y of the stress tensor. c)comparison of analytical and numerical solution $\theta = 0$. d) Volumetric plastic deformation

The building of the stress cage can be easily appreciated on the figure 5.5 where it is shown the Mohr circle of all the injection stages modelled under these conditions. It is clear how as the wellbore pressure increases the Mohr circle are expanding, nevertheless, looking closely to the circle of the last stage (green curve) it can be appreciated how the tangential stress is greater

that in the previous stage. This means that when the rock approximates to the transition between the strain hardening and the perfectly plastic material, the tangential stress start to build up. This behavior can be attributed to the fact that the all stress states above the failure envelop are unreachable for the rock, therefore it can stretch to lower values. If this was the only factor once reached this point of strain hardening, then the tangential stress should remains fixed while the radial stress increase with the wellbore pressure. The building of stress is also consequence of the dilatancy of the rock, since the rock is undergoing plastic deformation, the volume is increasing (as shown in chapter 2), however, the rock is in a highly confined environment (high pressure fluid in one direction and the surrounding rock in all other) then, some stress is build due to the increase of volume.

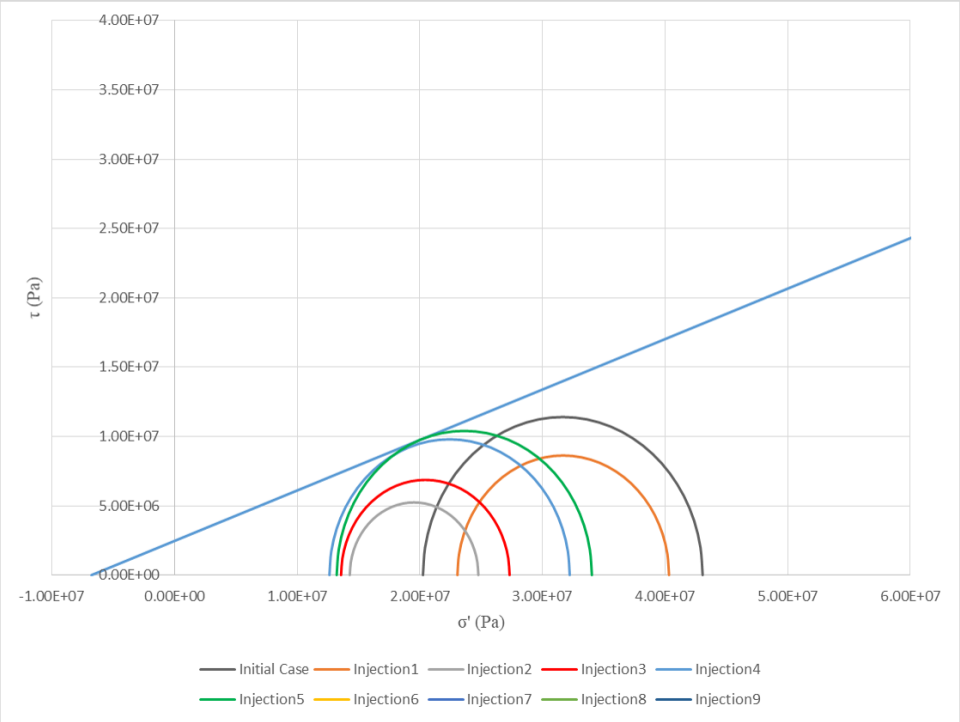


**Figure 5.5:** Case 2: Plastic Material. Horizontal Stress Anisotropy @2997.5m, Pw=62MPa. $S_0$plastic = 3Mpa. All Mohr Circles generated for the different injection stages

In reality it is unlikely to find a rock under real circumstances that presents a hardening strain behavior greater than a couple of megapascals. Nevertheless, in this project, it will tested a theoretical rock that exhibits that kind of behavior aiming to understand under which circumstances the fracture will initiate. The goal is to have an effective tangential stress at least equal to zero. In the previous case with an increment of one megapascal during the strain hardening the failure envelop remained to close stress state making the rock to build up the stress cage and not allowing to reach the tensile failure. On the next simulation the hardening rule it will increase $S_0$ plastic until 20MPa as follows:

| **Hardening factor** | $S_0$ **plastic (MPa)** |
|---|---|
| 0 | 2 |
| 0.01 | 20 |
| 0.1 | 20 |

**Table 5.4:** Hardening rule for case 2 ($S_0$ plastic until 20MPa)

Figure 5.6 shows similar results as in the previous case in a qualitative screening. In this case, several injection stages were added to the simulation in an attempt to reach the tensile failure. The stress distribution shown in figure 5.6a and b for a simulated mud weight of 62MPa shows a similar behavior as before. The real difference between this two cases is that the value in the hardening parameter and the effect of the different plastic deformation amount and stress build up due to plastic effects, as presented in table 5 and 6. For example for a wellbore pressure of 62MPa with a $S_0$ plastic de 3MPa the tangential stress was 42 MPa, meanwhile with a $S_0$ plastic of 20MPa the tangential stress is 39.3MPa (or $\sigma_\theta$= 9.93 MPa)

After increasing 10 times the $S_0$ plastic it was accomplished a decrease on the tangential stress, but this reduction is still far from the tensile failure criteria as shown in figure 5.7 where the mohr circles of this simulation are compared . It can be seen that as higher the wellbore pressure, the trangential stress tend to be closer together and as in the previous case scenario; for mud weight equal to 87MPa, the tangential stress is higher that for the previous step. So in the attempt of reaching the tensile failure, this was and step on the right direction but not quite enough by itself to accomplish the fracture initiation. Further increment on the strain hardening could be perform.

| | **Analytic Radial Stress (Pa)** | **Analytic Tangential Stress (Pa)** | **Analytic Tangential Stress (Pa)** | **Analytic Tangential Stress (Pa)** |
|---|---|---|---|---|
| Initial Case | 4.90E+07 | 7.25E+07 | 4.96E+07 | 7.25E+07 |
| Injection1 | 5.20E+07 | 6.95E+07 | 5.25E+07 | 6.97E+07 |
| Injection2 | 5.40E+07 | 4.05E+07 | 5.40E+07 | 4.31E+07 |
| Injection3 | 5.70E+07 | 3.75E+07 | 5.66E+07 | 4.16E+07 |
| Injection4 | 6.20E+07 | 3.25E+07 | 6.14E+07 | 3.93E+07 |
| Injection5 | 6.70E+07 | 2.75E+07 | 6.45E+07 | 3.77E+07 |
| Injection6 | 7.20E+07 | 2.25E+07 | 6.99E+07 | 3.80E+07 |
| Injection7 | 7.70E+07 | 1.75E+07 | 7.53E+07 | 3.76E+07 |
| Injection8 | 8.20E+07 | 1.25E+07 | 8.01E+07 | 3.70E+07 |
| Injection9 | 8.70E+07 | 7.51E+06 | 8.49E+07 | 3.63E+07 |

**Table 5.5:** Analytical and numerical solution for different injection stages case 2

| | **EpXX** | **EpYY** | **EpZZ** | **Hardening factor** | **$S_0$ plastic (MPa)** |
|---|---|---|---|---|---|
| Injection 2 | 2.30E-07 | 2.81E-04 | -1.38E-04 | 3.13E-04 | 2.56E+06 |
| Injection 3 | 7.51E-07 | 8.08E-04 | -3.96E-04 | 9.00E-04 | 3.62E+06 |
| Injection 4 | 1.58E-06 | 1.64E-03 | -8.06E-04 | 1.83E-03 | 5.29E+06 |
| Injection 5 | -4.78E-04 | 2.61E-03 | -7.97E-04 | 2.77E-03 | 6.98E+06 |
| Injection 6 | -1.00E-03 | 3.38E-03 | -7.98E-04 | 3.62E-03 | 8.51E+06 |
| Injection 7 | -1.65E-03 | 4.50E-03 | -7.98E-04 | 4.86E-03 | 1.08E+07 |
| Injection 8 | -2.30E-03 | 5.33E-03 | -7.98E-04 | 5.87E-03 | 1.26E+07 |
| Injection 9 | -2.94E-03 | 6.64E-03 | -7.98E-04 | 7.31E-03 | 1.52E+07 |

**Table 5.6:** Strain components X, Y and Z, hardening parameter and $S_0$ plastic case 2

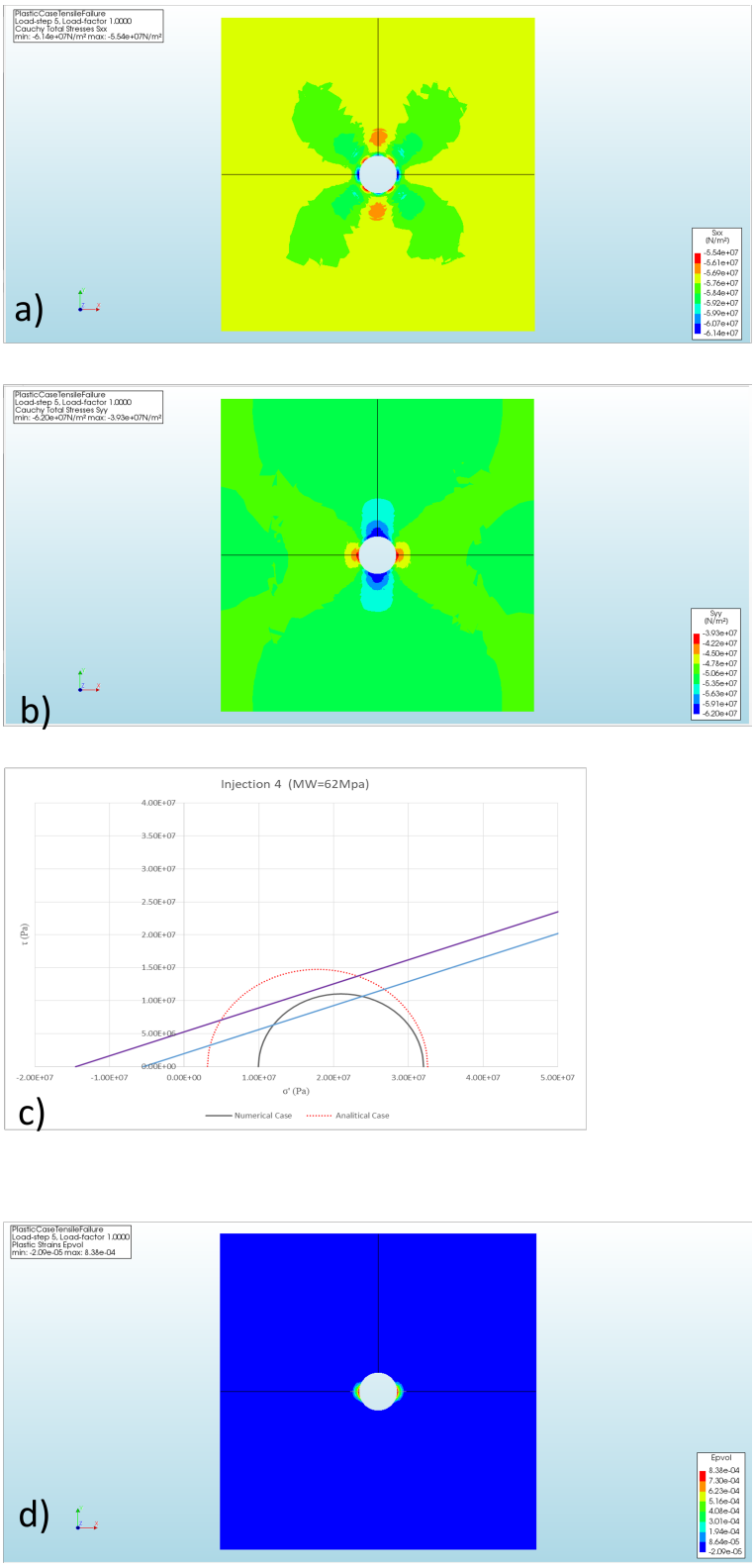


**Figure 5.6:** Case 2: Plastic Material. Horizontal Stress Anisotropy @2997.5m, Pw=62MPa. $S_0$plastic = 20Mpa. a) component X of the stress tensor. b) component Y of the stress tensor. c)comparison of analytical and numerical solution $\theta = 0$. d)Volumetric plastic deformation

For example increase even more the $S_0$ plastic, but having in consideration that greater values are unrealistic it does not add more value to the study. Other way could be to try change the friction angle of the rock and in this way achive a steeper slope of the failure envelop and

therefore higher chances of reaching the tensile failure. Nevertheless, a change in an intrinsic property of the rock as the fraction angle due to plastic deformation it will not be greater than a few degrees, and the implication wont be as big as need it to fulfill the tensile failure criteria.

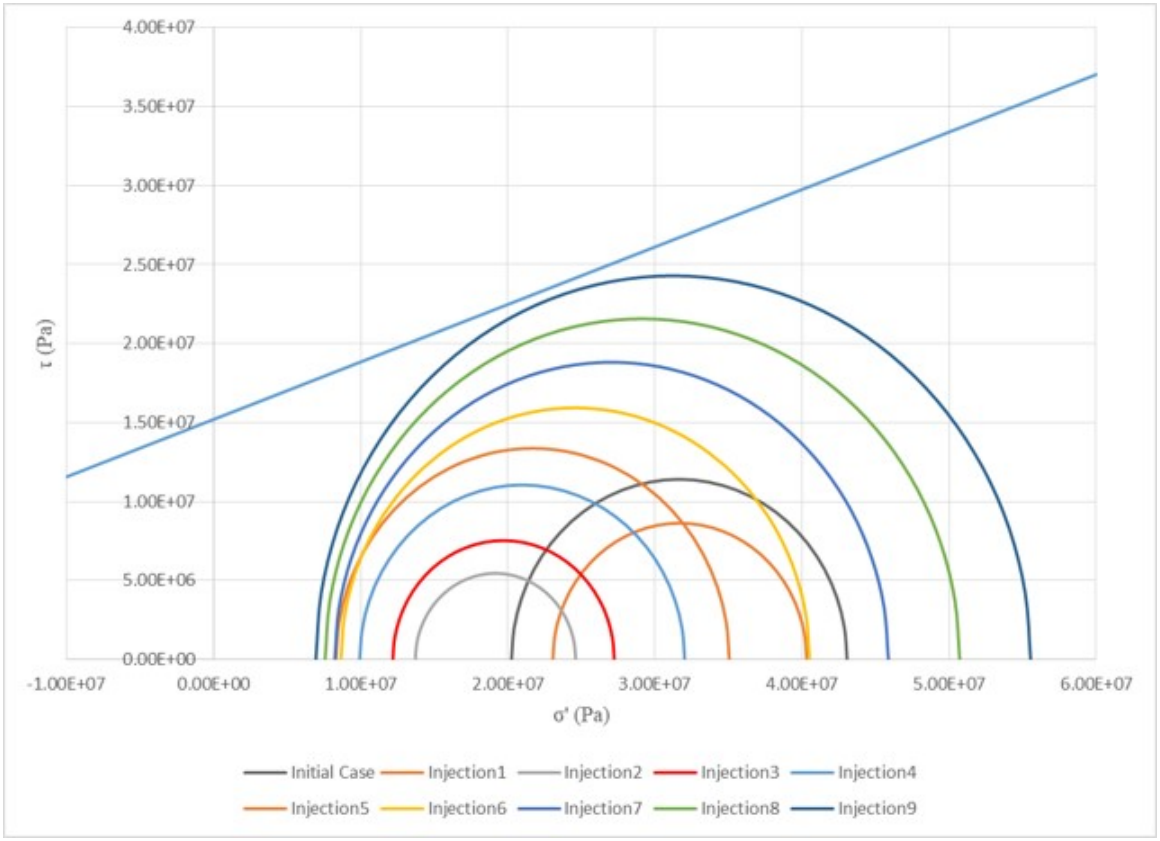


**Figure 5.7:** Case 2: Plastic Material. Horizontal Stress Anisotropy @2997.5m, Pw=62MPa. $S_0$plastic = 20Mpa. All Mohr Circles generated for the different injection stage

Finally, according to the simulations, is very unlikely to achieve the tensile failure in plastic material, then, during a hydraulic fracturing it has to be another factors that helps to the fracture initiation. This lies beyond the scope of the project, nevertheless among those factors it can be include in the model that the rock is a completely intact rock, in reality, the rock tends to be heterogeneous material with a lot of imperfections and small fracture or plane of weakness, as well as some defect on the fabric of the rock could help the fluid to percolate even a bit from the wellbore wall, and therefore, changing the stress field around the hole and transforming the issue from initiation to propagation of the fracture.

Another factor that plays in favor of fracture initiation is the change in pore pressure. Since the moment the well is drilled even for impermeable rock or if a perfect mud cake is build, the establishment of pressure equilibrium will occur as a function of time. The increment on pore pressure causes a reduction of the effective stresses and shifting the Mohr circle to the left making it closer to the tensile failure. An additional factor that could contribute in some extend to a fracture initiation is cooling effect between the treatment fluid and the formation by reducing the tangential stress.

## 5.3 Packer effect: Case 3

Another important factor during the minifrac test is the interaction between the packer and the formation. Some operator company has noticed that during some minifrac job is not possible to initiate the fracture, but if the packer is inflated and then moved the tool in a way that the zone that used to be in contact with the packer is now in the pressurized zone, it is much easier to initiate the fracture. The last simulation will try to give some insight into what could be occurring in the surrounding zone of the packer.

As reviewed in chapter 3 the packer needs to have a $\Delta P$ above the pressure of the zone between them. This means that for an undamaged rock the fracture it will be initiated on the packer zone. However, this fracture can not grow. Since there is no fluid on the packer the pressure at the fracture tip cant overcome the stresses around the hole.

As part of the modeling, the pressure of the packer was set to be increased in the same way as the reservoir zone in the previous run, from 51MPa to 76MPa. The pressure on the zone above and below the packers will remain constant at 49MPa and between the packers the pressure will be 2MPa lower than inside the packers.

Figure 5.8 shows a vertical slide on the X direction focused on the stress distribution, in which it can be easily appreciated the stress concentration along the borehole and especially in the packer zone due to the great differential pressure in this zone. Once the numerical model was made, it is interesting to take a look at the behavior of the deformation as shown in figure 5.9 where it can be observed the extent of the plastic zone. This zone as in the plastic case extend around 20 cm inside the formation.

On the other hand, when comparing the geometry against the extension of the plastic zone, it is clear how the plastic goes beyond the packer. Since the zones above the upper packer and below the lower packer have a low radial stress (if compared with the packer zone or between them) it could be created a condition low confining pressure in these zones, making possible to generate brittle failure. When moving the tool, the damage zone will be on the pressured interval making the fluid percolate into this imperfection. Once the pressurized fluid is beyond the wellbore wall initiate the fracture is much easier.

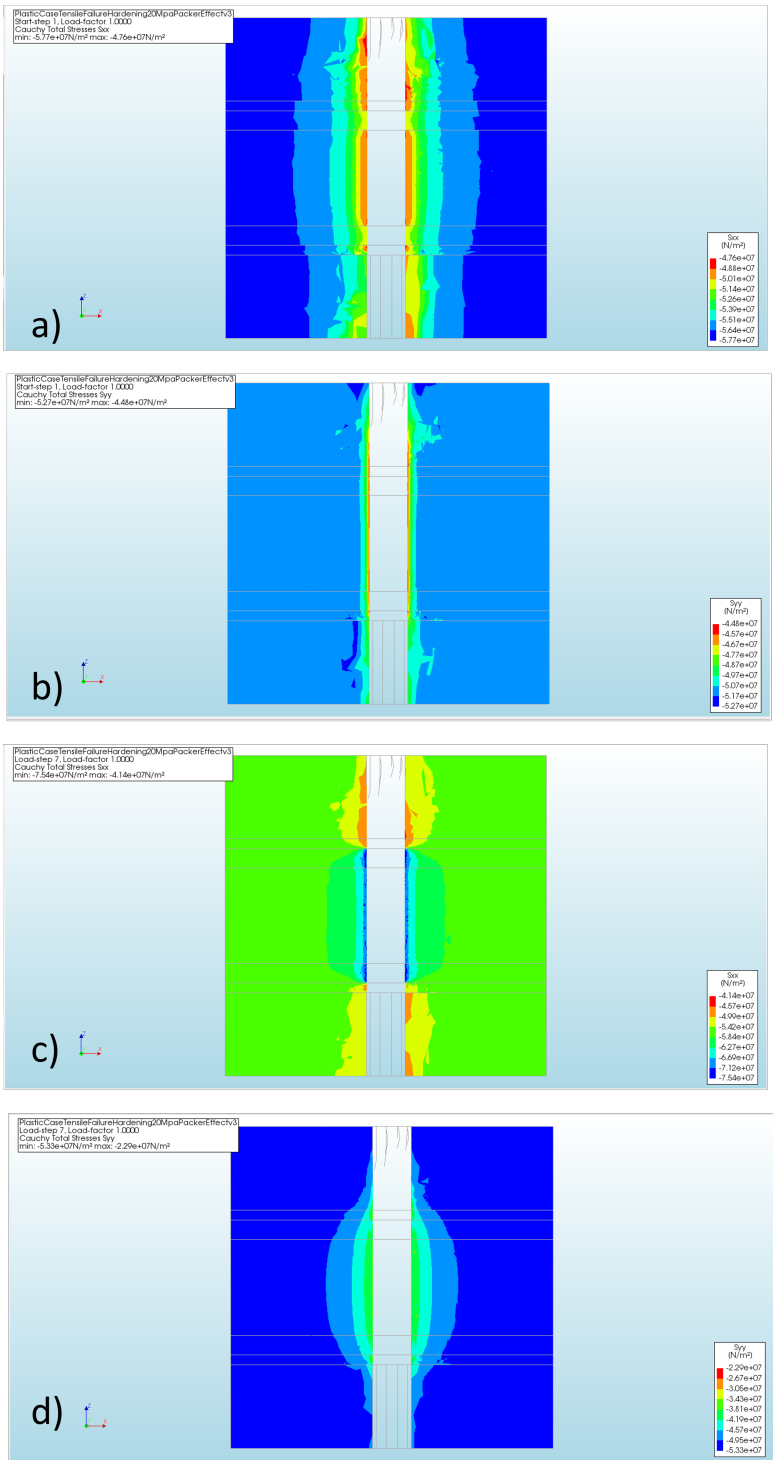


**Figure 5.8:** Vertical slide on the X direction a) component X of the stress tensor with PW = 49MPa. b) component Y of the stress tensor with PW = 49MPa. c) component X of the stress tensor with PW = 72MPa. d) component Y of the stress tensor with PW = 72MPa.

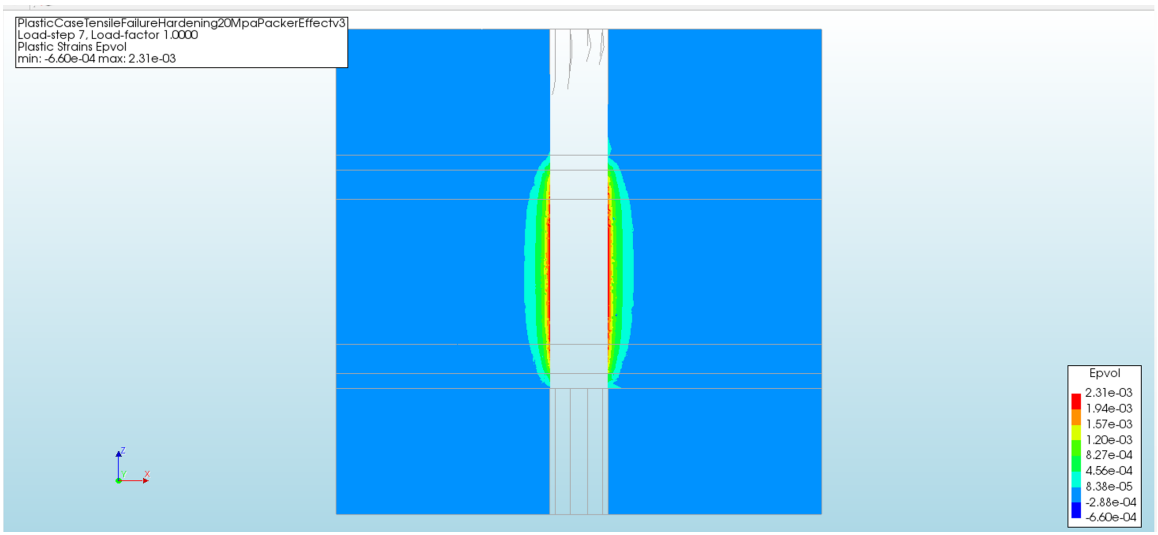


**Figure 5.9:** Vertical slide on the X direction showing volumetric plastic strain distribution

Chapter 6

# Conclusion

From the theoretical review is important to highlight the three main stages of the pressure decline curves. Being the first one when the fracture starts to close but the walls are not touching to each other, the second stage begins when the walls of the fracture start to be in contact to each other, the third stage, the fracture is already mechanically closed. The pressure decline on the first and last stages can be described as straight lines, which provide an upper and lower limits for the stress estimation. The second stage is much more complex and there is no analytical model capable to describe this process completely but this phase is quantitatively described as the changing of pressure, the fracture tip will close when the pressure inside the fracture is lower than the minimum horizontal stress and the fracture lip will remain open until the pressure at this point is greater than the hoop stress acting in the wellbore face.

Decline pressure behavior mainly depends on two principal elements, fracture stiffness, and leak-off rate. These two factors are competing with each other, and depending on which of them is predominant during the fracture close different interpretation techniques can be implemented to estimate the minimum horizontal stress. If the fracture closing process is dominated by the fracture stiffness, the system stiffness approach will give better results. Normally this technique will be used when rocks with low permeability or low leak-off rate were a conventional approach, so the pressure will take too long to decline. On the other hand, if the fracture closure is dominated by the formation leak-off, the G function approach can give more accurate results.

Regarding the second part of this work, the fracture initiation is a complex phenomenon with many variables taking place at the same time. In this project, the focus was in an aspect normally neglected in the hydraulic modeling as the plasticity behavior of the materials. To accomplish this objective a finite element analysis was performed simulating several wellbore pressures and analyzing the stress and strain response on the rock. During the modeling phase, the hardening rule was design such as the rock starts with a strain hardening when plastic deformation is reached until a certain amount of strain in which the hardening factor and therefore the strength will remain constant regardless of the deformation.

During the simulation it was shown that reaching the tensile failure criteria (negative effective or null tangential effective stress) is very unlikely by only changing the hardening rule. Even for an unrealistic material in which the strain hardening reached ten times the initial value, it was not possible to meet the criteria. The main cause for this behavior is the building of a stress cage in the neighborhood of the wellbore. It was shown that when the plastic strain get closer to the threshold in which the material will start to have a perfectly plastic behavior the

stress cage is such that the tangential stress instead of decreasing with each increase of the radial stress (as expected) start to build up, shifting the Mohr circle to the right and therefore further away of the tensile failure criteria. Then, to initiate the fracture others factors have to be take place at the same time, for instance, rock heterogeneities, plane of weakness and/or defects the fabric of the rock.

In case of any of the previous factors exist, it was shown by the simulation that by using the packers during a microfrac test, the zone where plastic deformation occurs extend beyond the packer itself. This plastic deformation in a zone with low confining stress created by the lower fluid pressure in the zones above and below the packers (mud weight) could cause brittle failure of the rock. Then, if this microfrac tool is moved in a way that those brittle failure zones are inside the interval to be pressured, this imperfection will cause perhaps a change in the hoop stresses distribution around the borehole or the increment of the pressure beyond the borehole wall, allowing fluid to penetrate into the formation. Either of those consequences will make that the fracture initiate despite the plastic behavior and the stress cage describe before. As a step forward, a laboratory test could be performed in order to check the results of the numerical simulation. The test can be carried out by submitting a sample with a vertical borehole in the center to a triaxial compression test.

# Bibliography


Alberty, M. W., McLean, M. R., et al., 2004. A physical model for stress cages. In: SPE annual technical conference and exhibition. Society of Petroleum Engineers.

Barree, R. D., Barree, V. L., Craig, D., 2007. Holistic fracture diagnostics.

Bower, A. F., 2009. Applied Mechanics of Solids. CRC press.

Bradford, I., Cook, J., et al., 1994. A semi-analytic elastoplastic model for wellbore stability with applications to sanding. In: Rock Mechanics in Petroleum Engineering. Society of Petroleum Engineers.

Bree, P. D., Walters, J. V., 1989. Micro/minifrac test procedures and interpretation for in situ stress determination. Int. J. Rock Mech. Min. Sci. Geomech 26 (6), 515–521.

Castillo, J., 1987. Modified fracture pressure decline analysis including pressure-dependent leakoff.

Charlez, P., et al., 1997. The impact of constitutive laws on wellbore stability: a general review. SPE Drilling & Completion 12 (02), 119–128.

Cheatham Jr, J., et al., 1967. Strain hardening of a porous limestone. Society of Petroleum Engineers Journal 7 (03), 229–234.

Chen, S., Abousleiman, Y., et al., 2016. An analytical solution for wellbore stability problem using strain hardening drucker-prager plasticity model. In: 50th US Rock Mechanics/Geomechanics Symposium. American Rock Mechanics Association.

Cornet, F. H., 2016. Hydraulic testing in boreholes for a robust and complete in situ stress determination. ISRM International Symposium on In-Situ Rock Stress 26 (6), 515–521.

Feng, Y., Arlanoglu, C., Podnos, E., Becker, E., Gray, K., et al., 2015. Finite-element studies of hoop-stress enhancement for wellbore strengthening. SPE Drilling & Completion 30 (01), 38–51.

Fjaer, E., Holt, R. M., Raaen, A., Risnes, R., Horsrud, P., 2008. Petroleum Related Rock Mechanics, 2nd Edition.

Han, G., Stone, T., Liu, Q., Cook, J., Papanastasiou, P., et al., 2005. 3d elastoplastic fem modelling in a reservoir simulator. In: SPE Reservoir Simulation Symposium. Society of Petroleum Engineers.

Hayashi, K., . H. B. C., 1991. Characteristics of shut-in curves in hydraulic fracturing stress measurements and determination of in situ minimum compressive stress. Journal Of Geophysical Research 96 (B11), 18,311–18,321.

Hill, R., 1950. The Mathematical Theory of Plasticity. OXford Classic text.

Howard, G. C., . F. C. R., 1957. Optimum fluid characteristics for fracture extension. American Petroleum Institute.

Ingraffea, A. P., Heuze, F. E., Ko, H.-Y., Gerstle, K., et al., 1976. Fracture propagation in rock: Laboratory tests and finite-element analysis. In: The 17th US Symposium on Rock Mechanics (USRMS). American Rock Mechanics Association.

J. C. Jaeger, N. G. C., Zimmerman, R. W., 2007. Fundamentals of Rock Mechanics, 4th Edition.

Kelly, P., 2013. Solid Mechanics Lecture Notes - An Introduction to Solid Mechanics. University of Auckland.

Michael J. Economides, T. M., 2007. Modern Fracturing Enhancing Natural Gas Production, 2nd Edition.

Nolte, K. G., 1979. Determination of fracture parameters from fracturing pressure decline. SPE Annual Technical Conference and Exhibition.

Nolte, K. G., 1986. A general analysis of fracture pressure decline with application to three models. SPE Form. Eval.

Nordgren, R., et al., 1972. Propagation of a vertical hydraulic fracture. Society of Petroleum Engineers Journal 12 (04), 306–314.

Pattillo, P. D., 1975. A modification of carters equation for fracture area. Fall Meeting of the Society of Petroleum Engineers of AIME.

Proskin, S., Scott, J., Chhina, H., et al., 1989. Interpretation of the minimum principal stress from microfrac tests. In: ISRM International Symposium. International Society for Rock Mechanics.

Raaen, A., Skomedal, E., Kjørholt, H., Markestad, P., Økland, D., 1991. Stress determination from hydraulic fracturing tests: the system stiffness approach. International Journal of Rock Mechanics and Mining Sciences 38 (4), 529–541.

Risnes, R., Garpestad, O., Gilje, M., Oland, L., Ovesen, M., Vargervik, E., et al., 1998. Strain hardening and extensional failure in high porosity chalk. In: SPE/ISRM Rock Mechanics in Petroleum Engineering. Society of Petroleum Engineers.

Sepehri, J., Soliman, M. Y., Morse, S. M., et al., 2015. Application of extended finite elementmethod to simulate hydraulic fracture propagation from orientedperforations. In: SPE hydraulic fracturing technology conference. Society of Petroleum Engineers.

Valkó, P., Economides, M., et al., 1997. Fluid leakoff delineation in high-permeability fracturing. In: SPE Production Operations Symposium. Society of Petroleum Engineers.

Vermeer, P. A., De Borst, R., 1984. Non-associated plasticity for soils, concrete and rock. HERON 29 (3).

# APPENDIX A: Injection stages for the model with $S_0$ plastic = 3MPa

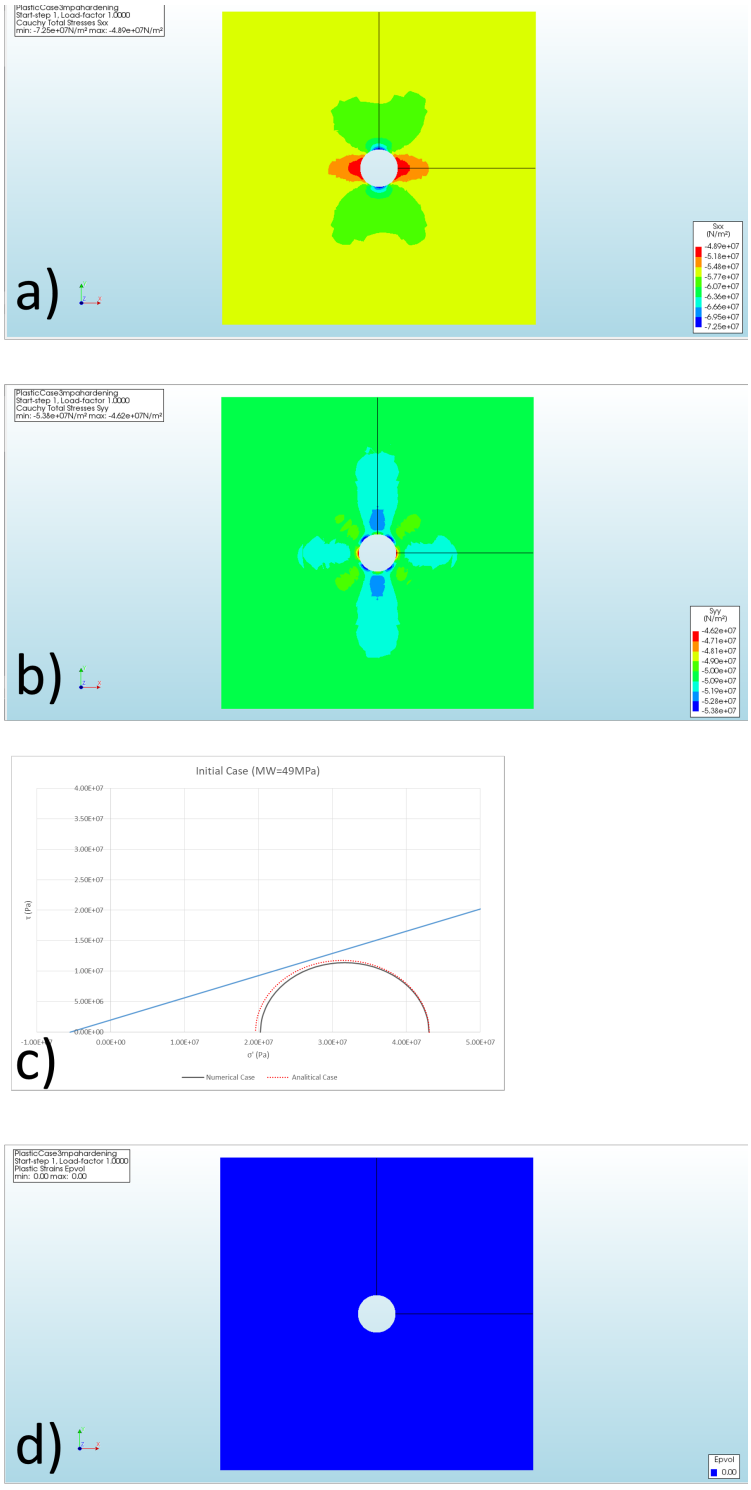


**Figure 6.1:** Wellbore Pressure 49MPa. $S_0$ plastic = 3Mpa. a) component X of the stress tensor. b) component Y of the stress tensor. c)comparison of analytical and numerical solution $\theta = 90$. d)Volumetric plastic deformation

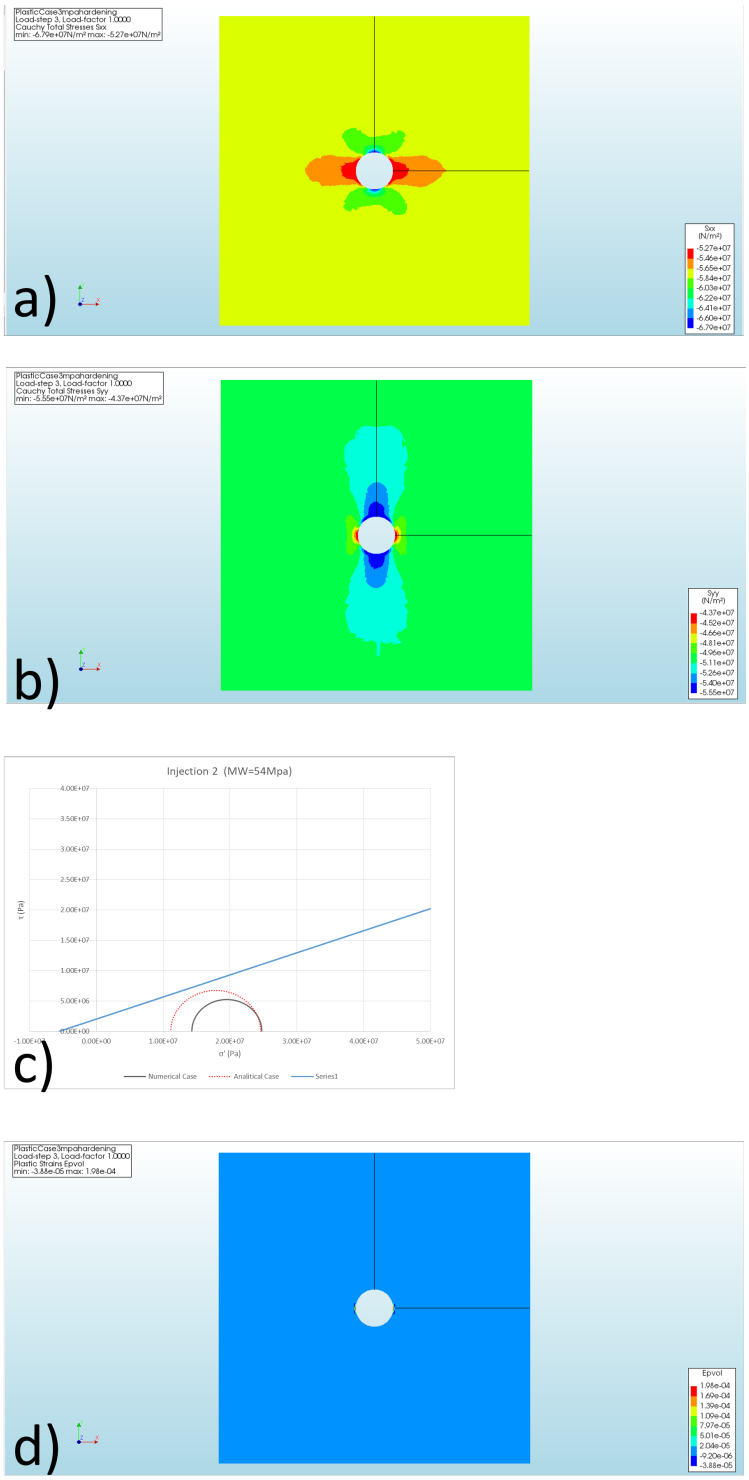


**Figure 6.2:** Wellbore Pressure 54MPa. $S_0$ plastic = 3Mpa. a) component X of the stress tensor. b) component Y of the stress tensor. c)comparison of analytical and numerical solution $\theta = 0$. d)Volumetric plastic deformation

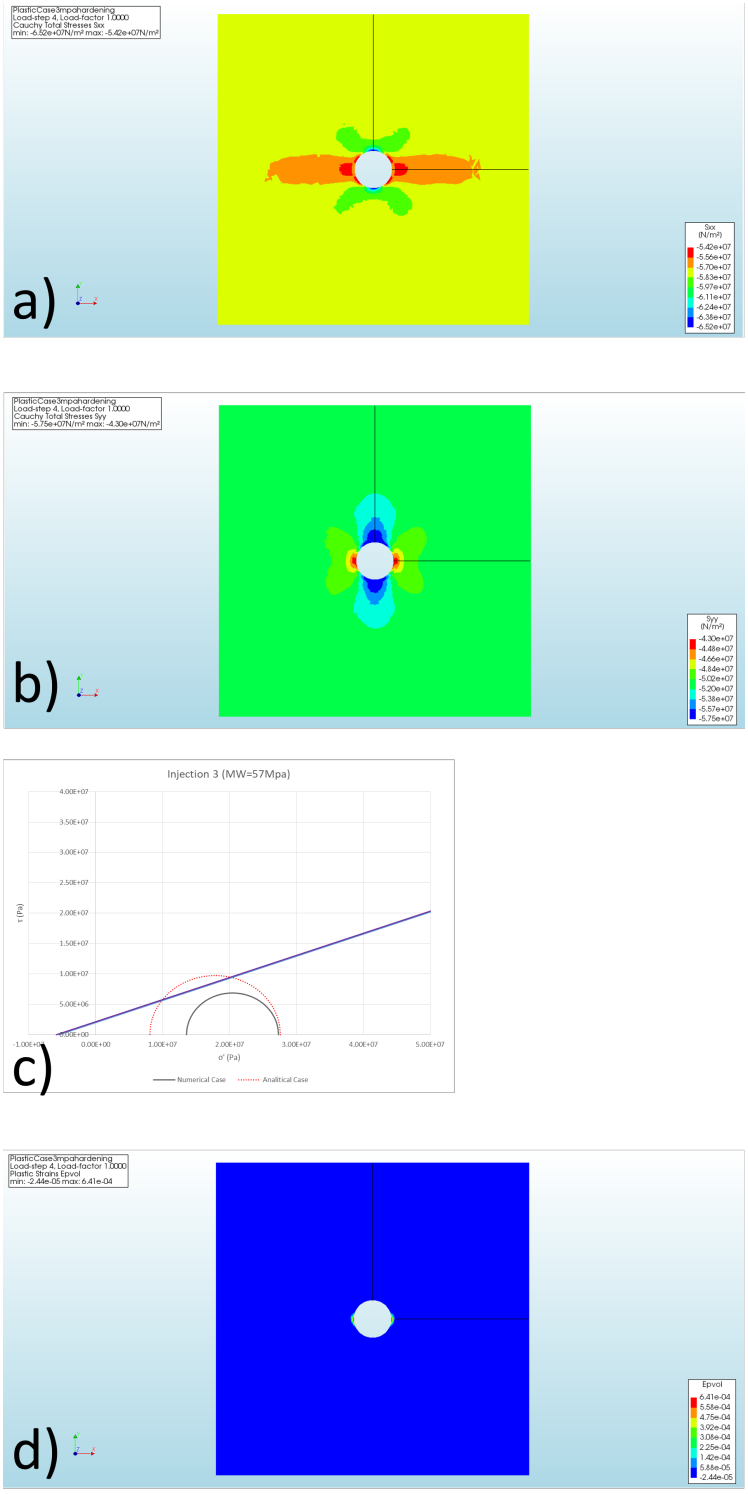


**Figure 6.3:** Wellbore Pressure 57MPa. $S_0$ plastic = 3Mpa. a) component X of the stress tensor. b) component Y of the stress tensor. c)comparison of analytical and numerical solution $\theta = 0$. d)Volumetric plastic deformation

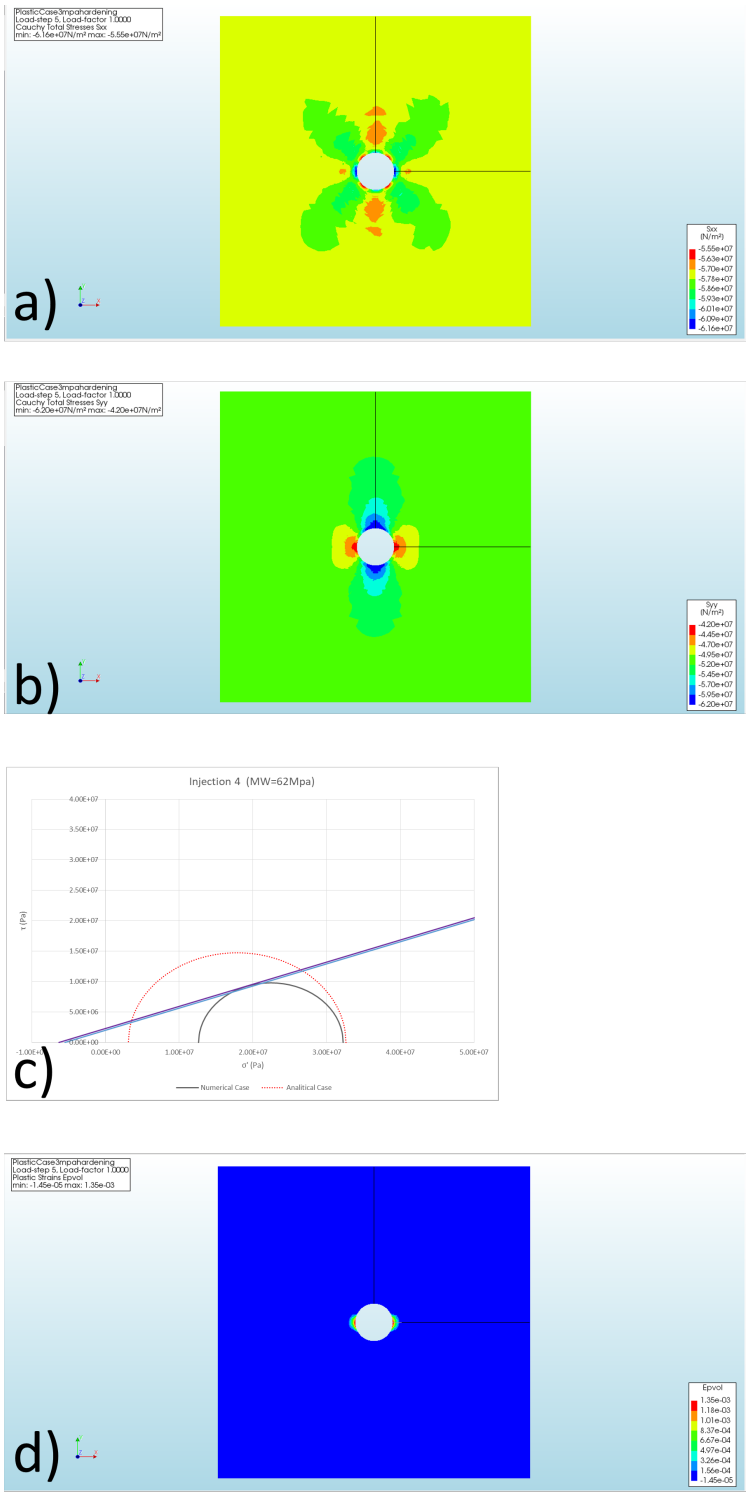


**Figure 6.4:** Wellbore Pressure 62MPa. $S_0$ plastic = 3Mpa. a) component X of the stress tensor. b) component Y of the stress tensor. c)comparison of analytical and numerical solution $\theta = 0$. d)Volumetric plastic deformation

# APPENDIX B: Injection stages for the model with $S_0$ plastic = 20MPa

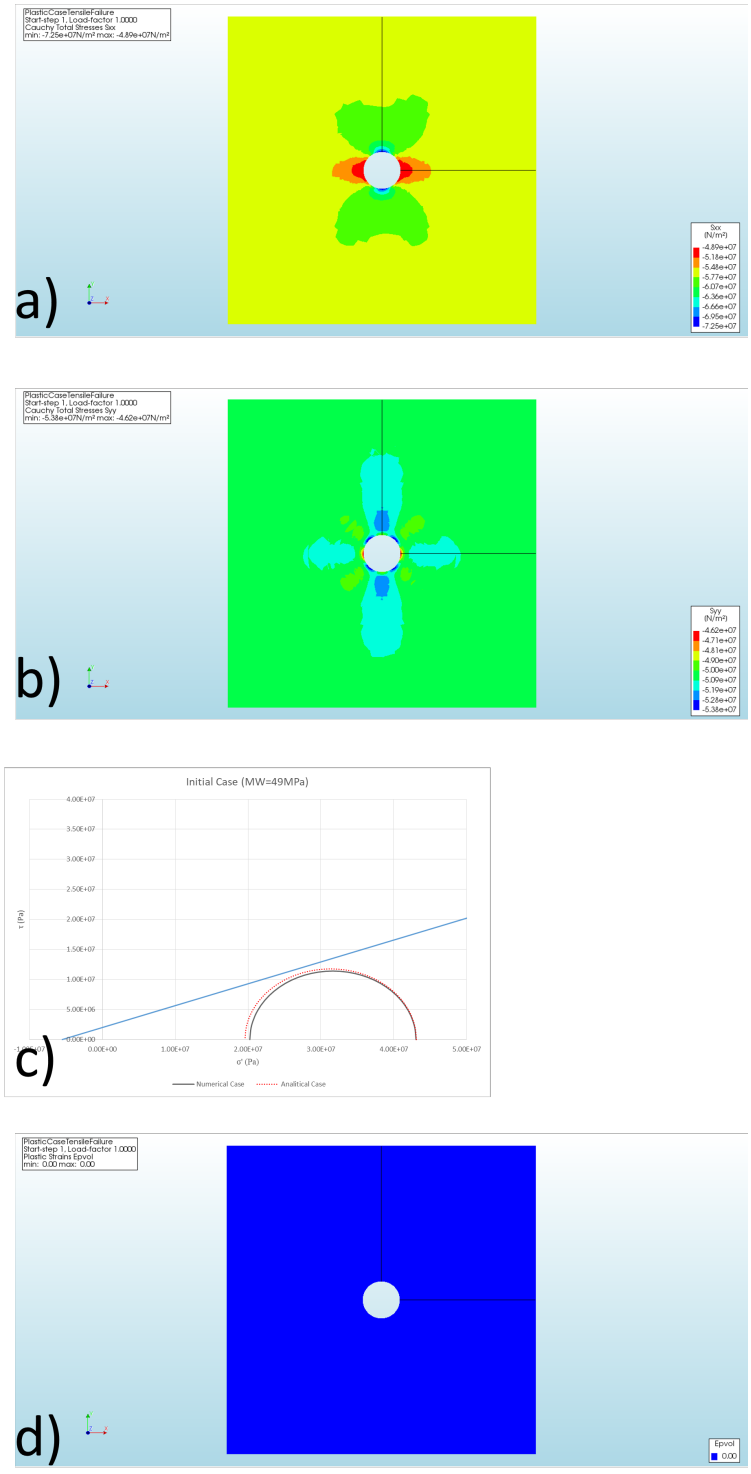


**Figure 6.5:** Wellbore Pressure 49MPa. $S_0$ plastic = 20Mpa. a) component X of the stress tensor. b) component Y of the stress tensor. c)comparison of analytical and numerical solution $\theta = 90$. d)Volumetric plastic deformation

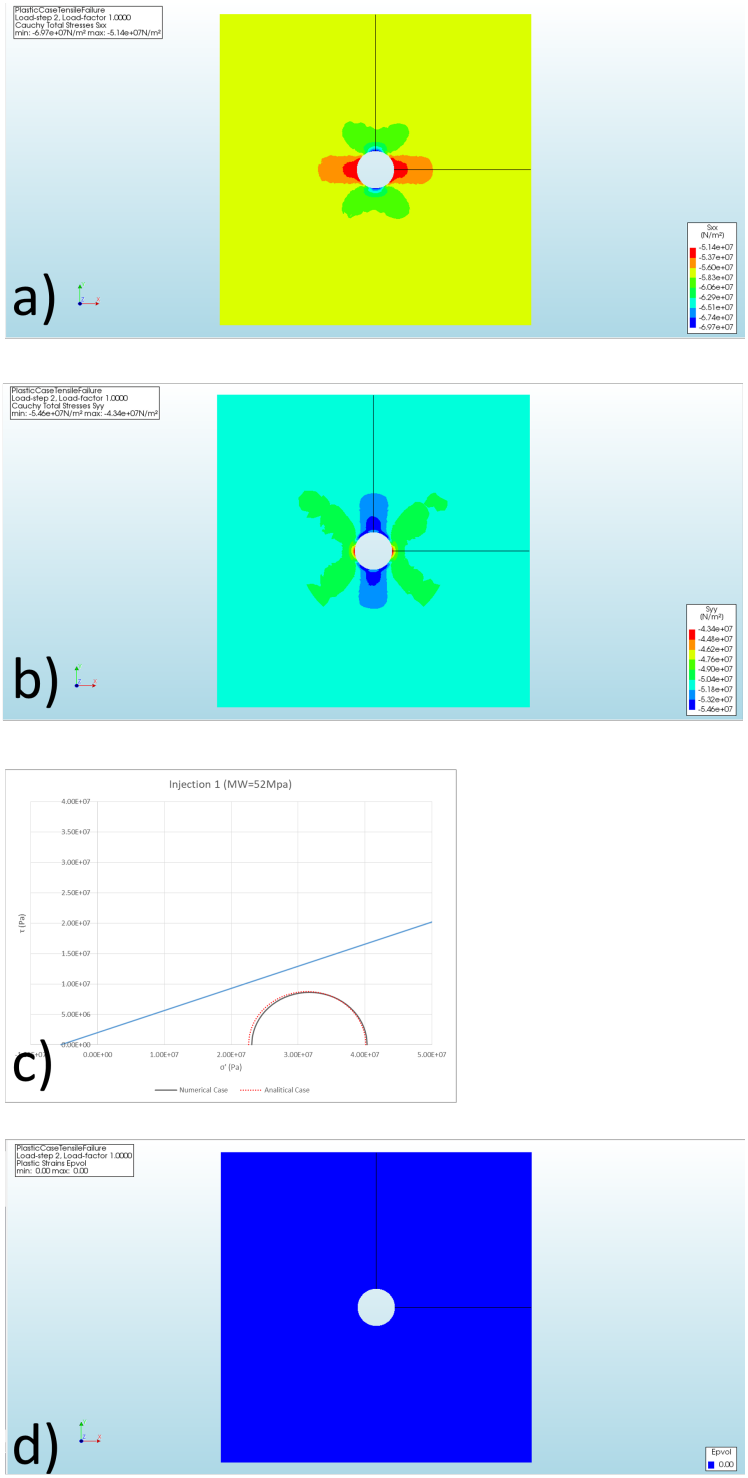


**Figure 6.6:** Wellbore Pressure 52MPa. $S_0$ plastic = 20Mpa. a) component X of the stress tensor. b) component Y of the stress tensor. c)comparison of analytical and numerical solution $\theta = 90$. d)Volumetric plastic deformation

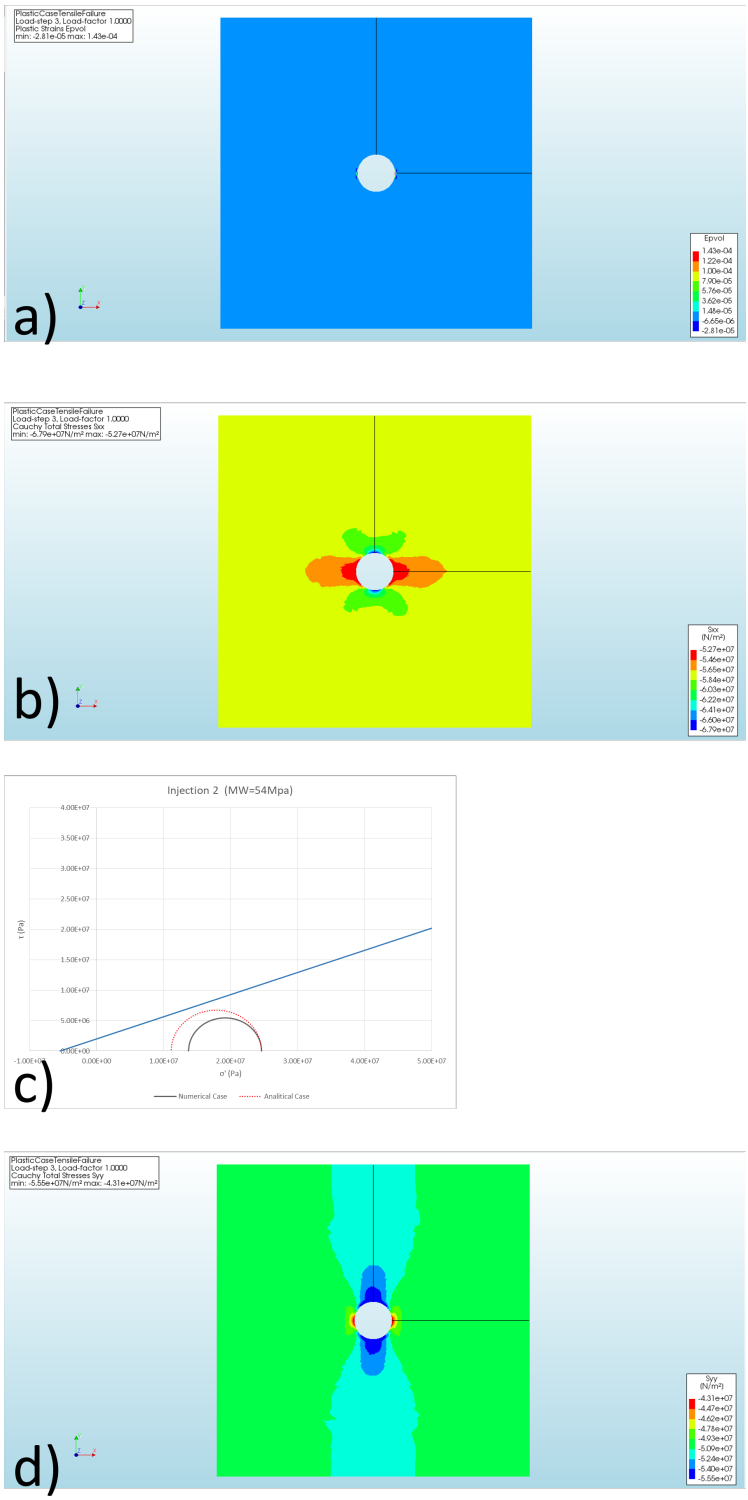


**Figure 6.7:** Wellbore Pressure 54MPa. $S_0$ plastic = 20Mpa. a) component X of the stress tensor. b) component Y of the stress tensor. c)comparison of analytical and numerical solution $\theta = 0$. d)Volumetric plastic deformation

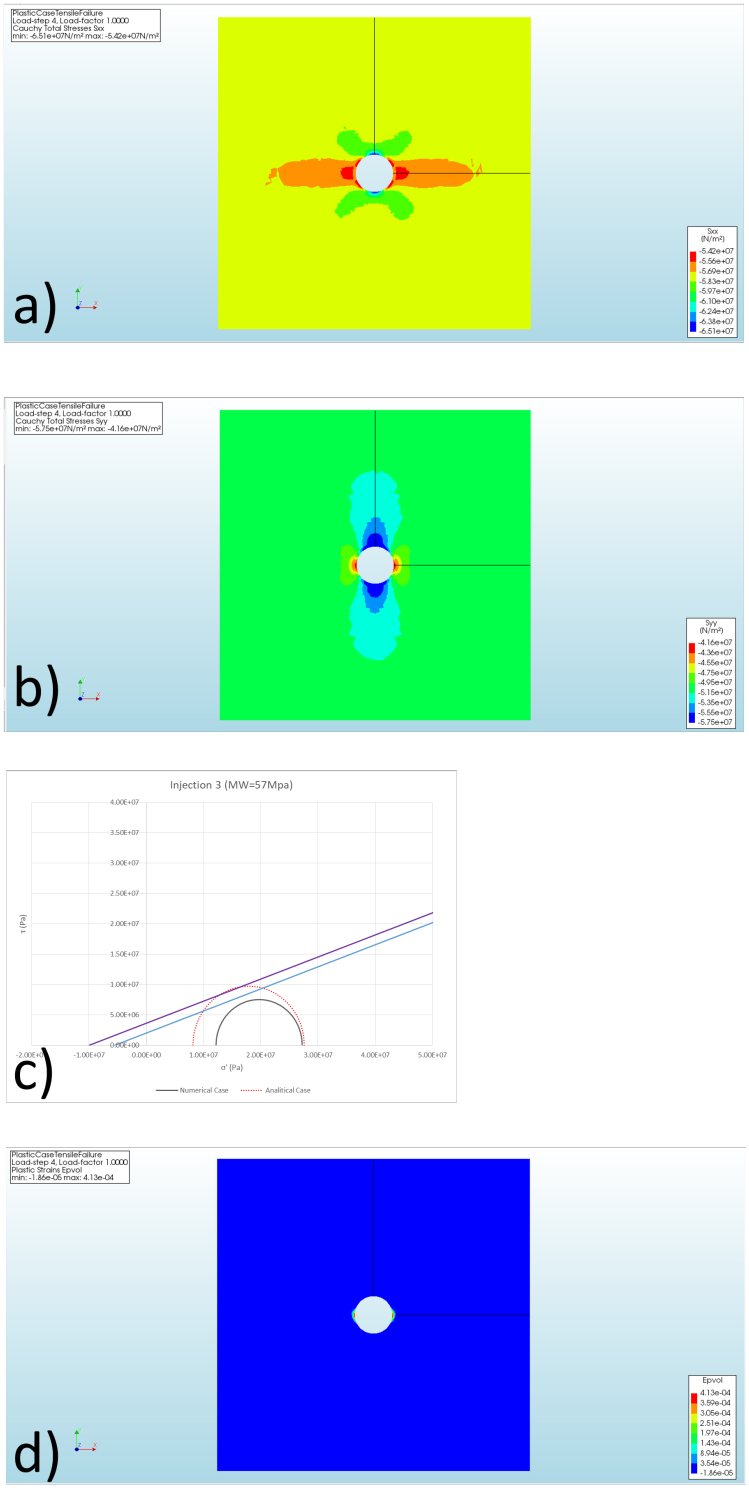


**Figure 6.8:** Wellbore Pressure 57MPa. $S_0$ plastic = 20Mpa. a) component X of the stress tensor. b) component Y of the stress tensor. c)comparison of analytical and numerical solution $\theta = 0$. d)Volumetric plastic deformation

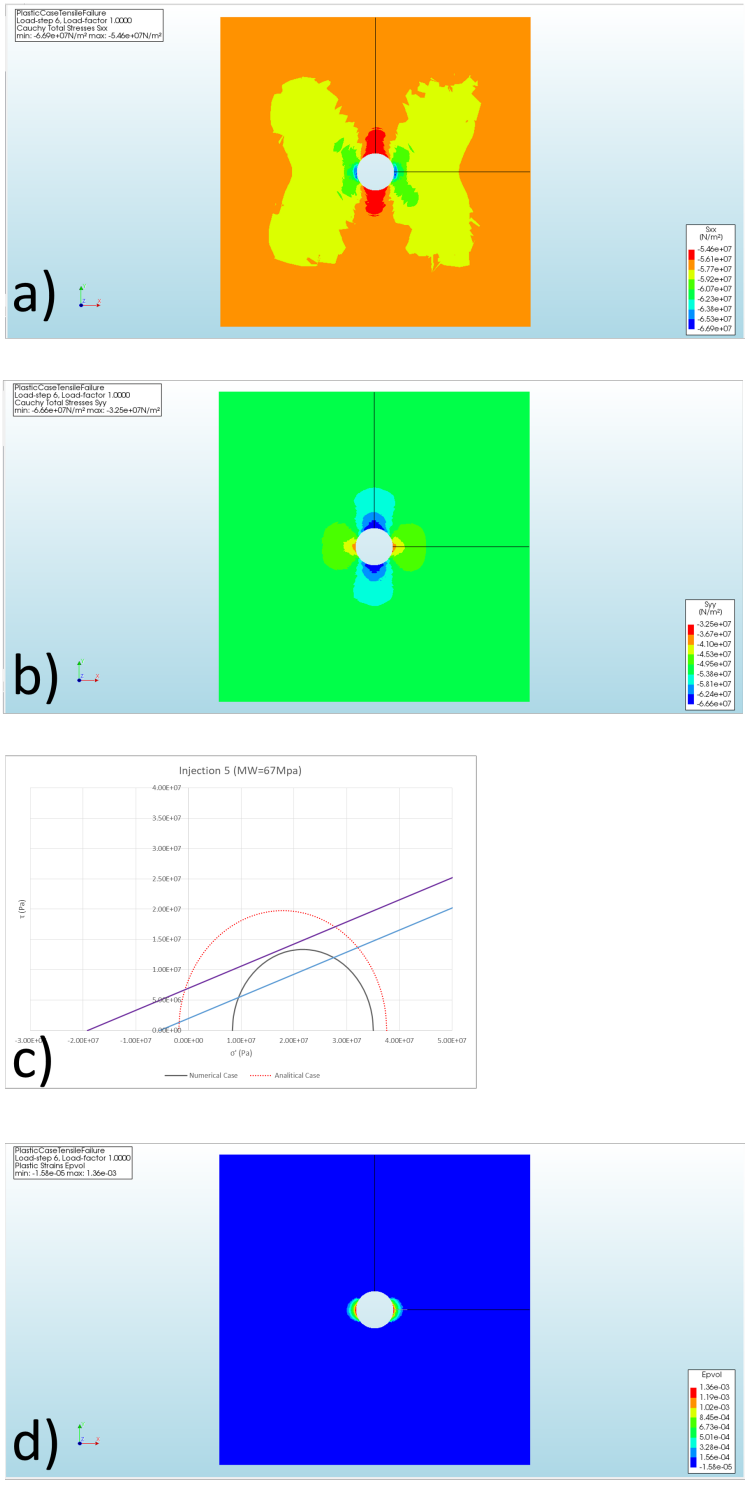


**Figure 6.9:** Wellbore Pressure 67MPa. $S_0$ plastic = 20Mpa. a) component X of the stress tensor. b) component Y of the stress tensor. c)comparison of analytical and numerical solution $\theta = 0$. d)Volumetric plastic deformation

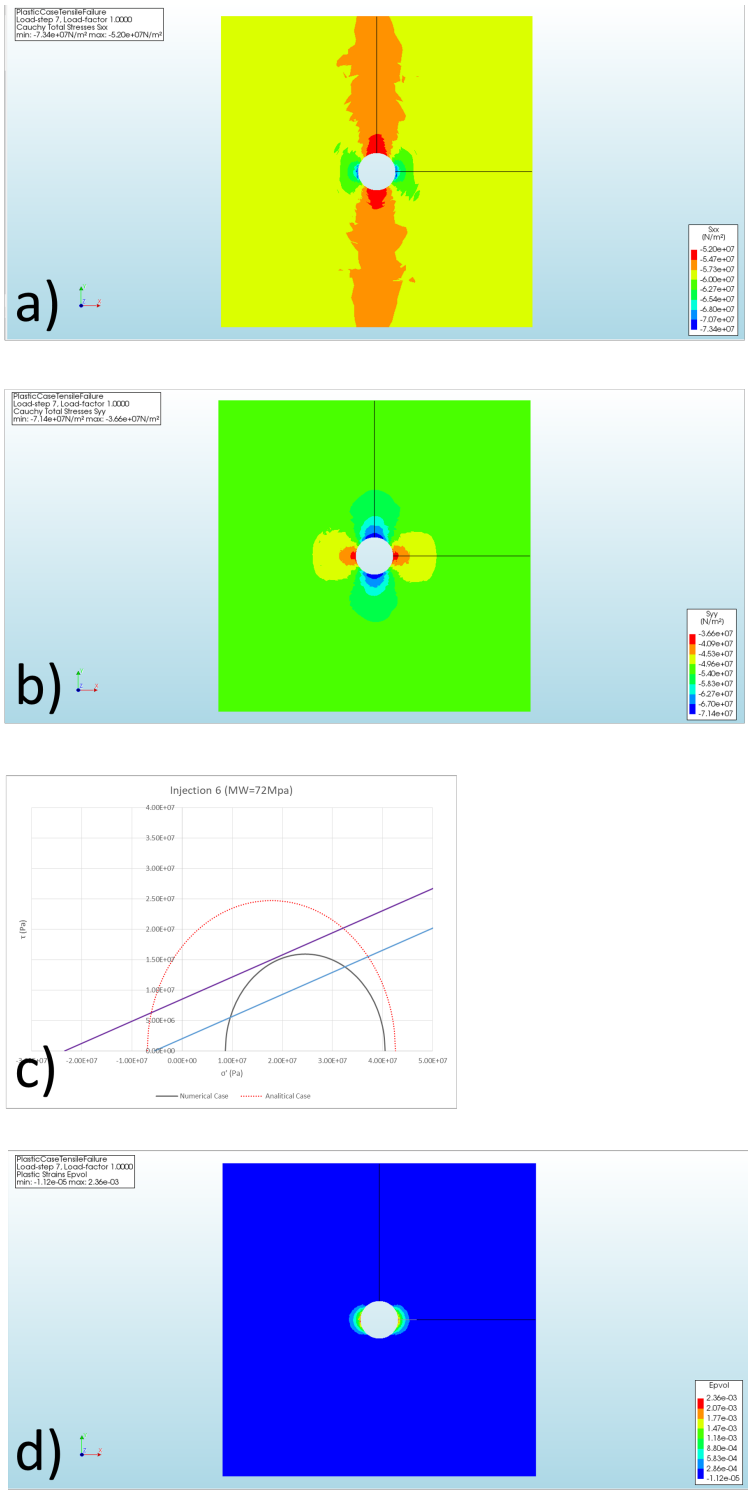


**Figure 6.10:** Wellbore Pressure 72MPa. $S_0$ plastic = 20Mpa. a) component X of the stress tensor. b) component Y of the stress tensor. c)comparison of analytical and numerical solution $\theta = 0$. d)Volumetric plastic deformation

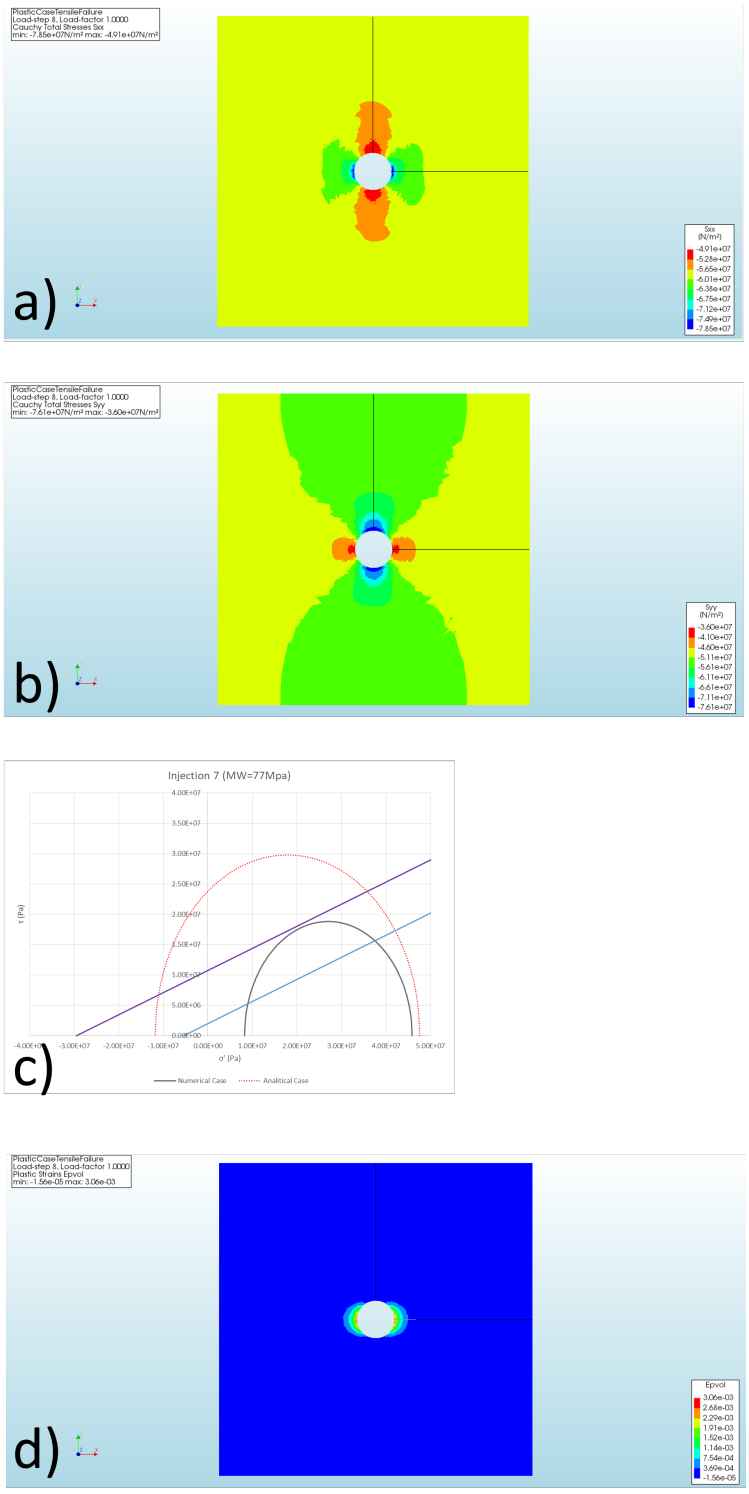


**Figure 6.11:** Wellbore Pressure 77MPa. $S_0$ plastic = 20Mpa. a) component X of the stress tensor. b) component Y of the stress tensor. c)comparison of analytical and numerical solution $\theta = 0$. d)Volumetric plastic deformation

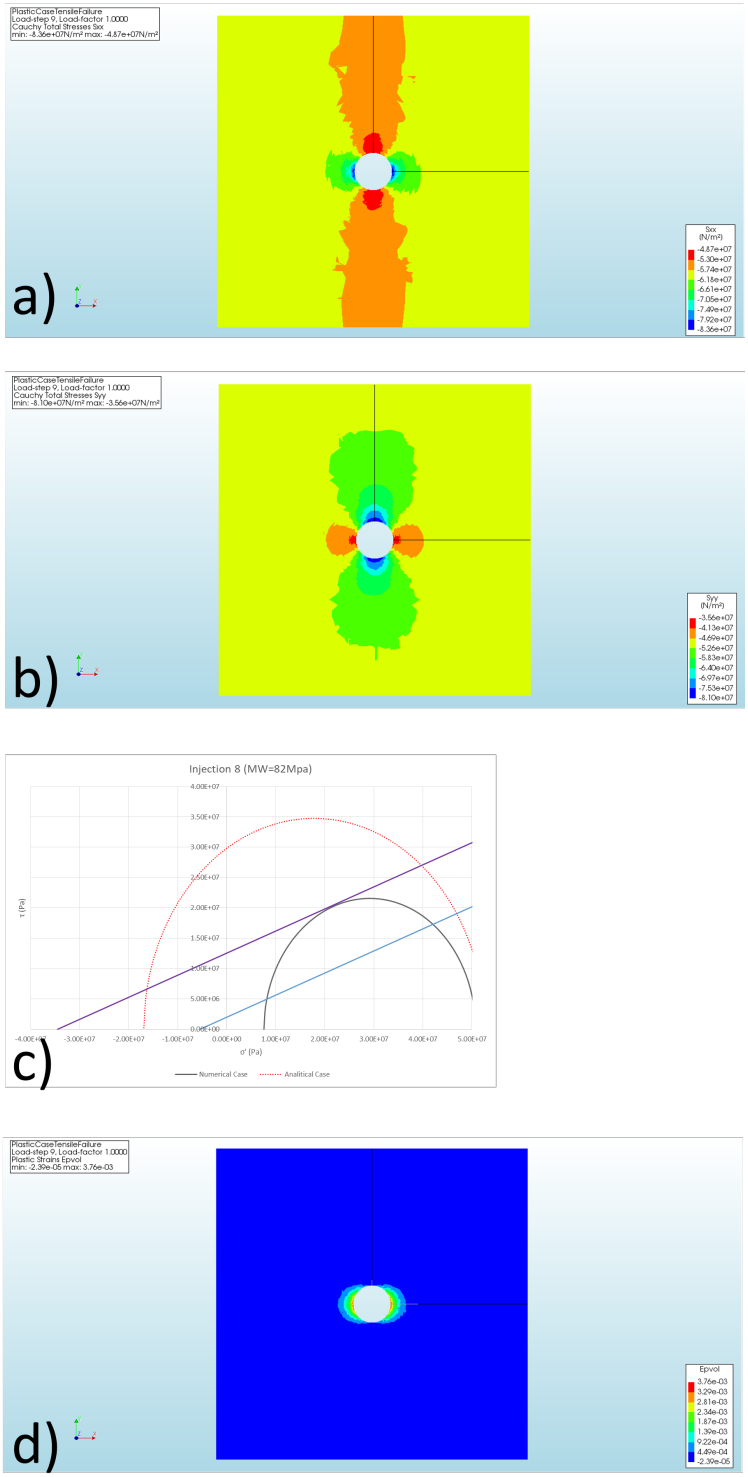


**Figure 6.12:** Wellbore Pressure 82MPa. $S_0$ plastic = 20Mpa. a) component X of the stress tensor. b) component Y of the stress tensor. c)comparison of analytical and numerical solution $\theta = 0$. d)Volumetric plastic deformation

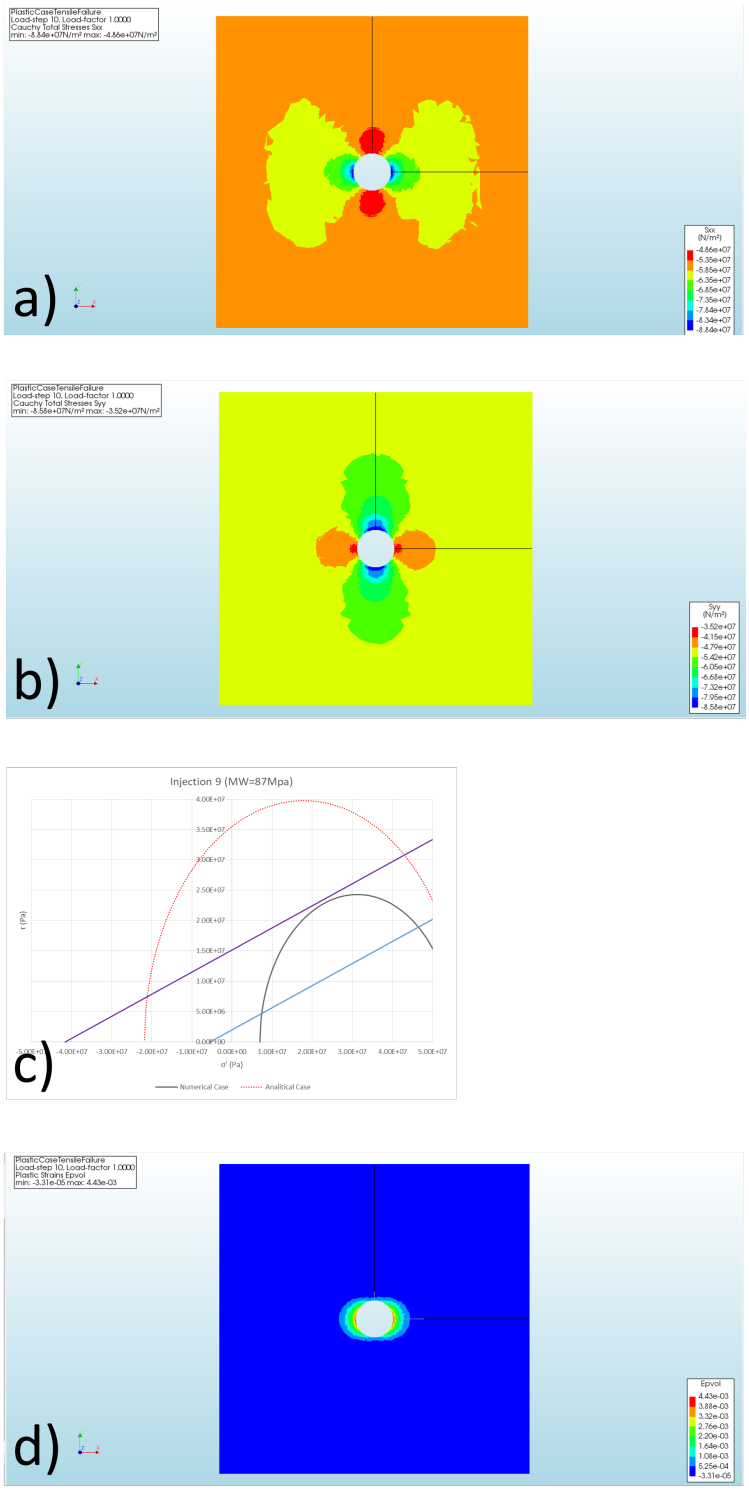


**Figure 6.13:** Wellbore Pressure 87MPa. $S_0$ plastic = 20Mpa. a) component X of the stress tensor. b) component Y of the stress tensor. c)comparison of analytical and numerical solution $\theta = 0$. d)Volumetric plastic deformation